

See discussions, stats, and author profiles for this publication at: <https://www.researchgate.net/publication/26877664>

# Metal Speciation Dynamics in Dispersions of Soft Colloidal Ligand Particles under Steady-State Laminar Flow Condition

ARTICLE *in* THE JOURNAL OF PHYSICAL CHEMISTRY A · OCTOBER 2009

Impact Factor: 2.69 · DOI: 10.1021/jp9068976 · Source: PubMed

---

CITATIONS

9

READS

30

## 2 AUTHORS:



[Jerome F.L. Duval](#)

French National Centre for Scientific Research

111 PUBLICATIONS 1,941 CITATIONS

[SEE PROFILE](#)



[Shizhi Qian](#)

Old Dominion University

156 PUBLICATIONS 2,515 CITATIONS

[SEE PROFILE](#)

# Metal Speciation Dynamics in Dispersions of Soft Colloidal Ligand Particles under Steady-State Laminar Flow Condition

Jérôme F. L. Duval<sup>\*,†</sup> and Shizhi Qian<sup>‡,§</sup>

*Laboratory Environment and Mineral Processing, Nancy-University, CNRS,  
BP 40 - F-54501 Vandoeuvre-lès-Nancy Cedex, France, Department of Aerospace Engineering,  
Old Dominion University, Norfolk, VA, and School of Mechanical Engineering, Yeungnam University,  
Gyongsan 712-749, South Korea*

Received: July 21, 2009; Revised Manuscript Received: September 16, 2009

A theory is presented for metal speciation dynamics in a swarm of soft, spherical core–shell colloidal ligand particles under steady-state laminar flow condition. Mass transfer and subsequent complexation of metal species within the reactive, permeable particle shell are governed by the interplay between (i) convective-diffusion of free metal ions M within and around the shell where ligands L are distributed, and (ii) kinetics of ML complex formation/dissociation in the shell. The local concentrations of metal M and complex ML are determined by the convective-diffusion equations with appropriate chemical source term and full account of radial and angular concentration polarization contributions. The steady-state flow field is determined from the solution of Navier–Stokes equation including convective acceleration term for the fluid external to the particle, and from Brinkman equation for the internal fluid flow. The confined location of ligands within the particle shell leads to ML formation/dissociation rate constants (denoted as  $k_a^*$  and  $k_d^*$ , respectively) that differ significantly from their counterparts ( $k_a$  and  $k_d$ ) defined for homogeneous ligand distribution throughout the solution. The relationship between  $k_{a,d}^*$  and  $k_{a,d}$  is derived from the numerical evaluation of the spatial, time-dependent distributions of free and bound metal within and/or outside the particle. The dramatic dependence of  $k_{a,d}^*$  on hydrodynamic particle softness, Péclet number, soft surface layer thickness, and particle radius are analyzed in the steady-state nonequilibrium chemical regime within the context of dynamic features for colloidal complexes. The analysis covers the limiting cases of hydrodynamically impermeable, hard particles where binding sites are located at the very surface of the particle core (e.g., functionalized latex colloids) and free draining, polymeric ligand particles devoid of a hard core (e.g., porous gel particles). The formalism further applies to any values of the Péclet number, that is, for speciation dynamics determined by kinetic processes coupled to diffusion and/or convection metal mass transfer(s). A discussion is provided for the comparison between the exact numerical results and the analytical formulation based on the approximate Levich expression for convective-diffusion metal flux at the surface of hard ligand particles.

## 1. Introduction

In natural systems, biotic and abiotic particles, such as bacteria and humic acids, are known to impact on the binding, transport, and fate of vital and toxic compounds like heavy metals, thereby controlling their circulation in the various environmental compartments.<sup>1,2</sup> The processes underlying the reactivity of particles with respect to metal ions are generally not at equilibrium<sup>1</sup> but either in some steady-state or subject to change in time. For the sake of illustration, the response of microorganisms to environmental pollutants or nutrient metal species is determined by a chain of intertwined dynamic events, each of them characterized by specific spatial and temporal scales: transfer of metal species to and from the biological surface and chemical conversion of those into bioactive form in the close vicinity of the surface, followed by transport across the membrane and internalization (bioputake) and possibly excretion.<sup>3</sup> It is now increasingly accepted that appropriate understanding of metal speciation in aquatic media necessarily requires in-depth analysis of the coupling between the relevant

mass transport modes(s) of metal to and from the consuming surface together with the kinetic features of interconversion of metal complex species.<sup>1</sup> Such dynamic approach allows a quantitative connection between the various physicochemical forms of metal species and their mobility, toxicity, or bioavailability.<sup>4,5</sup>

In aquatic media, the situation is extremely intricate because metal species can bind to a wide spectrum of ligand entities, ranging from small dissolved inorganic or organic ions, colloidal (bio)particles, aggregates, or biofilms, all defined by distinct physicochemical properties, for example, in terms of size, mass, charge, or hydrodynamic permeability. One of the major distinction between, for example, colloidal ligand particles and ligand molecules/ions is that the binding sites for the former are confined within the particle geometry whereas, for the latter, ligands may be viewed as point-like entities homogeneously distributed throughout the solution. Only few studies have specifically addressed the peculiarities of metal speciation in dispersions of colloidal ligand particles in connection with the constrained localization of the binding sites.<sup>6–10</sup> Pinheiro et al.<sup>6</sup> quantitatively showed that ignoring the spatial confinement of carboxyl ligands at the surface of hard latex particles may lead to a dramatic overestimation of the formation rate of lead and

\* Corresponding author.

† Nancy-University.

‡ Old Dominion University.

§ Yeungnam University.

cadmium colloidal complexes and to significant misinterpretation of their dynamic and lability properties,<sup>6,7</sup> in agreement with experimental data. Recently, Duval et al.<sup>9,10</sup> reported a comprehensive formalism for the most general situation of metal speciation dynamics in dispersions of soft colloidal ligand particles. Such particles, which consist of a hard core surrounded by a charged, ion-permeable shell layer, generally better describe particles of environmental relevancy such as humics, microorganisms, or mineral particles covered by adsorbed organic layers.<sup>11</sup> The results discussed in the first two publications of this series<sup>9,10</sup> showed that the dynamic and lability properties of colloidal metal complexes are generally determined by a complex coupling between conduction and diffusion of metals to and from the soft particle together with the kinetics of interconversion of metal species within the reactive shell. As a result of these mixed transport/kinetic processes taking place inside and/or outside the particle, the dynamic properties of colloidal ligand complexes are necessarily dependent on the core-to-shell ratio, the particle size, or the spatial distribution of ligand sites within the particle shell volume.<sup>9,10</sup> The details of the interphasial particle electric double layer, as determined by the particle charge and medium composition (pH, ionic strength), were further shown to govern the electrically driven transport of free metal ions within and outside the particle, thus determining for a part the overall metal flux to the particle and therefore the dynamic properties of the formed colloidal complex.<sup>10</sup>

In environmental systems like rivers, oceans, and soils, the formation of colloidal metal complexes issued from interaction between metals and ligand particles and their circulation generally takes place under flow conditions. In other contexts, at the current age of micro- and nanotechnology based applications, flowing mixtures within channels are separated/analyzed via the monitoring of a signal which reflects the rate of reaction involving the targeted elements and sensing colloidal entities (e.g., (bio)particles) located at the channel surface. The basic understanding of such mixed kinetics-convective diffusion controlled reactions at (bio)surfaces calls for a detailed, comprehensive physicochemical analysis. In the current paper, we extend our previous reports by examining metal speciation dynamics in dispersions of soft colloidal ligand particles under steady-state laminar flow condition. Because the particle shell where ligands are distributed is permeable to (metal) ions and fluid flow,<sup>12,13</sup> it is anticipated that the details of the flow field not only outside but also within the ligand particles are crucial in governing dynamics of metal speciation. The results discussed in this paper corroborate the above anticipation and further demonstrate for the first time the intimate relationship between dynamics of metal complexes formed with soft ligand colloids and their so-called hydrodynamic softness, that is, their propensity for fluid flow penetration.

## 2. Theory

**2.1. Formulation of the Problem.** Adopting the nomenclature introduced in our previous reports,<sup>9,10</sup> we consider a dilute dispersion of soft colloidal ligand particles consisting of a core of radius  $a$ , strictly impermeable to solvent molecules, ions, and fluid flow, and a soft, permeable shell of thickness  $d$  (Figure 1). The particles are dispersed in an aqueous medium where metal ions are introduced at a bulk concentration denoted as  $c_M^*$ , as illustrated in Figure 1 and further detailed in section 2.3. It is merely assumed that the metal ions M can interact with ligand sites L according to the following reversible 1:1 reaction

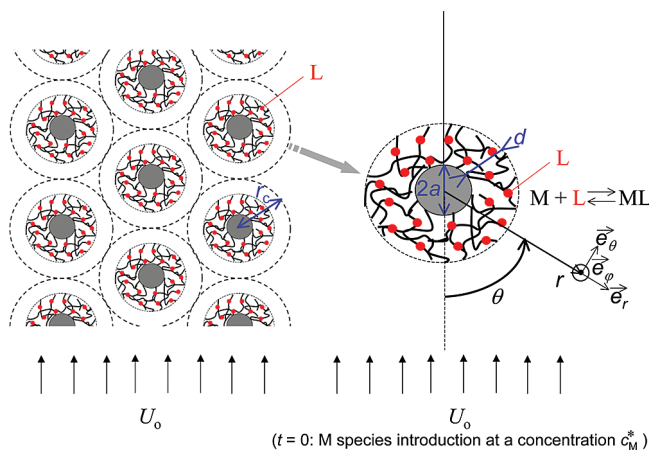


**Figure 1.** Scheme (not to scale) of a dispersion of monodisperse soft colloidal ligand particles distributed according to a Kuwabara cell type representation<sup>9,10</sup> under laminar flow conditions. The nomenclature adopted in the analysis is specified. The formalism detailed in section 2 is applicable for dilute particle suspension, that is,  $r_c > a + d$ .

where ML stands for the formed complex and  $k_a$  and  $k_d$  are the intrinsic complex formation and dissociation rate constants, respectively. The ligands L are homogeneously distributed within the particle shell and are present at a constant concentration denoted as  $c_L^*$ . The magnitude of the rate constant  $k_a$  is generally in agreement with Eigen mechanism.<sup>6–10,14–16</sup> In detail, this mechanism depicts the forward association reaction in eq 1 as the succession of two steps. First, the hydrated metal ion interacts with the ligand L to form a so-called outer-sphere complex, and the equilibrium stability constant of such a reaction is usually denoted as  $K_{os}$ . Then, following this outer-sphere ML complex formation, a water molecule is removed from the inner coordination sphere of the metal ion at a rate constant denoted as  $k_w$ . According to Eigen mechanism, which has been proven to hold over a wide variety of metal and ligands, the formation of the outer-sphere complex is a fast initial step, and it is then the removal of the first water molecule in the inner metal hydration sphere that determines the overall rate of the complex formation reaction. Accordingly, the constant  $k_a$  is written as  $k_a = K_{os}k_w$ .<sup>6–10,14–16</sup> As extensively argued by Buffle et al.,<sup>17</sup> the outer-sphere complex formation may however become, under certain conditions, the rate limiting step in the forward reaction of eq 1. This is particularly true, for example, for colloidal ligand particles with large density of complexing sites.<sup>17</sup> Following this observation, Buffle and co-workers defined a generalized Eigen expression for the constant  $k_a$  where dynamics of both outer-sphere complex formation and water removal steps are accounted for. In cases where the overall complex formation is severely limited by the water removal step, the generalized Eigen expression for  $k_a$  then reduces to  $k_a = K_{os}k_w$ , which is the conventional limit discussed above. Without loss of generality, we shall consider in this study  $k_a$  values evaluated on the basis of the latter expression, recalling that data for  $K_{os}$  and  $k_w$  are accessible in the literature for a number of metals and ligands.<sup>15</sup> In the current analysis, we examine quantitatively the importance of fluid convection in governing dynamics of metal speciation in soft colloidal ligand dispersions. Doing so, the basis of metal ion transport to and from the particle-confined ligands is concomitantly provided by diffusion and liquid flow within and around the permeable particle. The conditions which ensure the validity and applicability of our theoretical formalism are expressed below. For the sake of completeness, some of them, already specified and extensively discussed in refs 9 and 10, are briefly recalled.

• (i) Steady-state flow convection is envisaged, with  $U_0$  the relative velocity of the bulk liquid with respect to the soft ligand particle. Fluid dynamics is tackled for Reynolds numbers ( $Re$ ) sufficiently small so that laminar flow condition prevails. Recalling that  $Re$  is defined by  $Re \sim U_0(a + d)/\nu$  with  $\nu$  the kinematic viscosity of the medium, the latter condition safely applies for  $Re < < 2500$ . It allows us neglect turbulence effects on metal transport.

• (ii) Colloidal ligand dispersions are sufficiently dilute to ignore the overlap of diffusion layers developing around adjacent particles and the effects of particle crowding on flow field distribution. In line with this, depletion of metal ion concentration from the bulk value  $c_M^*$  reached far from the ligand particle is not considered.

• (iii) We exclude the impact of particle sedimentation on convective diffusion of metal species. This leads to the definition of an upper size limit for the particle dimension of about 1–10  $\mu\text{m}$  above which the model reported below can not be applied.<sup>9,10</sup> Additionally, the particle Brownian motion is viewed as immaterial for the derivation of the flow field distribution and the dynamics of metal speciation. Stating differently, we consider cases where characteristic times of colloidal transport by diffusion are infinitely long as compared with those relevant for the dynamics of molecular interaction between M and L. For Péclet numbers so low that metal transport is essentially ensured by diffusion (situation met for sufficiently small  $U_0$ ), the above assumption remains satisfied on the premise that a lower-size limit for the particles  $\sim 2\text{--}5$  nm is defined.<sup>9,10</sup> Also, the dynamics of motion for the polymer segments supporting the ligand sites is disregarded.<sup>9,10</sup>

• (iv) Within the scope of the current analysis, the medium contains a large excess of indifferent background electrolyte over the M species, which avoids the necessity to account for impacts of particle electric double layer on metal speciation dynamics, as addressed specifically in the second publication of this series.<sup>10</sup>

• (v) Finally, in conforming to situations of practical interest,<sup>6–10</sup> there is an excess of particle binding sites as compared with free metal in solution, that is,  $c_L^* > c_M^*$  where  $c_L^*$  is the time- and space-independent concentration of ligands distributed homogeneously within the particle shell.

In situations where the soft colloidal ligand particles are microorganisms, refined consideration of particle geometry, kinetics of reaction, and metal internalization steps are surely required. Despite the obvious limits of our model for predicting the fate of metal species in communities of such living bioparticles, the basic physical arguments related to the importance of finite flow penetration within the ligand (bio)particle on speciation dynamics still remain applicable. It is thereby recalled that recent analyses of electrokinetic properties of (bio)environmental ligand particles, such as humic acids,<sup>18</sup> polysaccharides,<sup>19</sup> bacteria,<sup>20</sup> yeast cells,<sup>21</sup> and viruses,<sup>22</sup> now allow determination of their hydrodynamic permeability.

**2.2. Fluid Dynamics in Dispersion of Soft Colloidal Ligand Particles.** In the following, the local two-dimensional flow velocity field within/outside the particle shell is represented by the vector quantity  $\vec{u}(r,\theta) = u_r(r,\theta)\vec{e}_r + u_\theta(r,\theta)\vec{e}_\theta$ , where  $(r,\theta)$  are the spherical coordinates with reference taken at the center of the particle core, and  $(\vec{e}_r, \vec{e}_\theta)$  defines the unit vector system (Figure 1). The symmetry of the problem imposes that hydrodynamics (and concentration polarization, see section 2.3) is independent of the azimuthal angle  $\varphi$ . For incompressible Newtonian fluid, the steady-state velocity profile  $\vec{u}(r,\theta)$  within the particle shell is provided by the Brinkman equation that reads

$$a \leq r \leq a + d: \nabla \bullet \{-pI/\eta + [\nabla \vec{u} + (\nabla \vec{u})^\top]\} - \lambda_o^2 \vec{u} = \vec{0} \quad (2)$$

where  $\eta$  is the dynamic viscosity of the medium,  $I$  is the identity tensor of order 2,  $p$  is the pressure, and  $\lambda_o$  is the so-called hydrodynamic softness of the ligand particle.<sup>12,13</sup> The symbols  $\nabla \bullet$  represents the divergence operator, and  $\nabla$  represents the gradient operator in polar coordinates. The quantity  $1/\lambda_o$  has length dimension and reflects the typical penetration of fluid flow within the shell component of the particle. The friction coefficient  $k_o$ , which stands for the drag exerted by the particle shell on the fluid flow, is connected to  $1/\lambda_o$  via the relation  $k_o = \eta \lambda_o^2$ .<sup>12,13</sup> The permeability coefficient  $\sigma$ , as sometimes introduced in equations governing flow field distribution in porous media, is given by  $\sigma = \lambda_o^{-2}$ . The term between brackets on the left-hand side of eq 2 represents the hydrodynamic stress tensor with pressure and viscous components. The second term in eq 2 stems from the porous, permeable nature of the shell composed of polymer chains that exert viscous drag on the flow. Quantitatively, the expression of  $\lambda_o$  as a function of polymer segment concentration may be found from Brinkman formalism<sup>23</sup> that relates the friction coefficient  $k_o$  to the hydrodynamic polymer volume fraction  $\phi_o$  in the shell according to a nonlinear expression.<sup>13</sup> The quantity  $\phi_o$  is given by  $\phi_o = 4\pi n_o a_s^3 / 3$  where  $n_o$  is the polymer segment density and  $a_s$  is the radius of the resistance center of the polymer chains as introduced by Debye-Bueche<sup>24</sup> in their formalism which assimilates the porous polymeric shell to a collection of spheres of radius  $a_s$  that exert frictional forces on the flow. For sufficiently low water content within the shell, typically  $\phi_o < 0.3$ , the Brinkman relation may be linearized with, as a final result,  $\lambda_o = [9\phi_o/(2a_s^2)]^{1/2}$ .<sup>13,25</sup> Recent experimental and theoretical work on electrokinetics of permeable, thermoresponsive thin-films demonstrated the adequacy of Debye-Bueche and Brinkman formulations for hydrodynamics in porous media of high water content.<sup>26</sup> For systems where  $\phi_o > 0.3$ , evaluation of  $\lambda_o$  or equivalently of the permeability  $\sigma$  necessarily requires taking into account the nonlinear terms involved in the Brinkman equation.<sup>13,23</sup> Alternatively, the permeability may be determined using other models as derived by Kim-Russel,<sup>27</sup> Happel,<sup>28</sup> Neal and Nader,<sup>29</sup> or Carman,<sup>30</sup> all based on Debye-Bueche<sup>24</sup> representation of flow within random array of hydrodynamically interacting spheres with fixed spatial configuration.

Outside the shell particle, the local flow velocity field is determined by the steady-state Navier–Stokes equation

$$r \geq a + d: \nabla \bullet \{-pI/\eta + [\nabla \vec{u} + (\nabla \vec{u})^\top]\} - \nu^{-1}(\vec{u} \cdot \nabla \vec{u}) = \vec{0} \quad (3)$$

with  $\nu = \eta/\rho$  the kinematic viscosity of the medium and  $\rho$  the fluid density. The second term in eq 3 denotes the fluid convective acceleration (or fluid flow dispersion term), that is, the acceleration of the fluid as it passes around the particle. For low Reynolds number  $Re$ , this term is insignificant as compared with that related to viscous and pressure forces. When the flow is a fully developed laminar flow, the convective acceleration may be ignored. As we shall detail in the following, although the flow is fully developed laminar flow far away from the particle, it is strongly distorted in the vicinity of the latter. The flow is then spatially dependent (and two-dimensional) in the region near the particle, and the inertial term in eq 3 should be taken into account. In view of this and considering that values

of  $Re$  up to 1 are considered in this study, we used the complete formulation of Navier–Stokes equation which includes inertial term.

In our analysis, we shall examine speciation dynamics in particle dispersions under flow conditions corresponding to Péclet numbers  $Pe \sim U_0(a + d)/D_{M,out}$  (with  $D_{M,out}$  as the diffusion coefficient of metal M outside the particle) in the range  $10^{-1}$ – $10^3$  and Reynolds number of about  $10^{-4}$  to 1 at most. It is emphasized that the choice of the length scale ( $a + d$ ) in the expression of the Péclet number of the here considered point-like ion is motivated by arguing that particle size is involved in the classical expressions of the radial diffusional flux for an ion toward a spherical particle<sup>9,10</sup> and in that of the diffusion layer thickness in the vicinity of a hard particle. Obviously, the mathematical formulation of the flow problem given by eqs 2 and 3 applies to cases of a particle moving through a stagnant liquid and that of a particle with fixed spatial position in a flowing liquid.

The steady-state flow is axial-symmetric with respect to the plane ( $r,\theta = 0$ ) so that the relevant computational spatial domain may be restricted to  $\theta \in [0,\pi]$ . The continuity equation for the fluid motion (mass conservation) within and outside the particle imposes that

$$r \geq a: \nabla \cdot \vec{u} = 0 \quad (4)$$

Far from the particle, the local fluid velocity field should match bulk liquid velocity so that

$$\vec{u}(r \rightarrow \infty, \theta) \rightarrow \vec{u}_o = (-U_o \cos \theta, U_o \sin \theta) \quad (5)$$

The no-slip condition at the surface of the impermeable particle core is further written

$$\vec{u}(r = a, \theta) = \vec{0} \quad (6)$$

The required continuity conditions for the radial and tangential velocity components at the position  $r = a + d$ , marking the transition between particle shell and solution, lead to

$$u_r(r = \{a + d\}^+, \theta) = u_r(r = \{a + d\}^-, \theta) \quad (7)$$

$$u_\theta(r = \{a + d\}^+, \theta) = u_\theta(r = \{a + d\}^-, \theta) \quad (8)$$

Finally, the radial and tangential components of the hydrodynamic stress tensor, denoted as  $\sigma_{rr}$  and  $\sigma_{r\theta}$ , respectively, depend on the local flow velocity according to  $\sigma_{rr} = -p + 2\eta \partial u_r / \partial r$  and  $\sigma_{r\theta} = \eta[\partial u_r / (r \partial \theta) + \partial u_\theta / \partial r - u_\theta / r]$  and must be continuous at  $r = a + d$ , that is,

$$\sigma_{rr}(r = \{a + d\}^+, \theta) = \sigma_{rr}(r = \{a + d\}^-, \theta) \quad (9)$$

$$\sigma_{r\theta}(r = \{a + d\}^+, \theta) = \sigma_{r\theta}(r = \{a + d\}^-, \theta) \quad (10)$$

Equations 2–10 fully determine the spatial distribution for the flow field inside the porous shell and outside the soft particle, that is, in surrounding medium.

**2.3. Transport Equations Governing the Time-Dependent Local Concentrations of Metal M and Complex ML Species within and/or Outside Soft Ligand Particles.** Within the framework of the model specified in section 2.1, and under the hydrodynamic conditions detailed in section 2.2, metal species M are introduced in the medium far away from the soft colloidal ligand particle at a concentration  $c_M^*$  (Figure 1). This operation defines our reference time, that is,  $t = 0$ . Under the conditions outlined in section 2.1, the mass conservations for M and ML are then given by the following convection-diffusion-reaction equations

$$\begin{cases} a \leq r < a + d: \\ \frac{\partial c_{ML}(t, r, \theta)}{\partial t} = -\{k_d c_{ML}(t, r, \theta) - k_a c_M(t, r, \theta) c_L^*\} \\ \frac{\partial c_M(t, r, \theta)}{\partial t} = D_{M,in} \nabla^2 c_M(t, r, \theta) + \\ \{k_d c_{ML}(t, r, \theta) - k_a c_M(t, r, \theta) c_L^*\} - \vec{u}(r, \theta) \cdot \nabla c_M(t, r, \theta) \end{cases} \quad (11, 12)$$

$$r \geq a + d: \frac{\partial c_M(t, r, \theta)}{\partial t} = D_{M,out} \nabla^2 c_M(t, r, \theta) - \vec{u}(r, \theta) \cdot \nabla c_M(t, r, \theta) \quad (13)$$

where  $c_{i=M,ML}(t,r,\theta)$  is the local concentration of species i at a given time  $t$  and polar coordinates  $(r,\theta)$ ,  $\nabla^2 F = 1/r^2 \partial[r^2 \times \partial F / \partial r] / \partial r + 1/(r^2 \sin \theta) \partial[\sin \theta \times \partial F / \partial \theta] / \partial r$  is the Laplacian operator in spherical geometry applied to a function  $F(t,r,\theta)$  and  $\vec{u}(r,\theta)$  is the steady-state flow velocity field determined in section 2.2. It is recalled that, under the conditions specified in section 2.1, the bulk metal concentration  $c_M^*$  outside the particle and the bulk concentration  $c_L^*$  of ligands within the shell are not depending on time  $t$  nor on space variables  $(r,\theta)$ .<sup>9,10</sup> The diffusion coefficient of free metal species within and outside the shell layer are denoted as  $D_{M,in}$  and  $D_{M,out}$ , respectively. For negligible electrostatic and steric interactions between free metal ions and sites supported by the polymer chains, the equality  $D_{M,in} = D_{M,out}$  is nearly satisfied.<sup>31</sup>

The initial conditions for M and ML are simply defined by

$$c_{ML}(t = 0, a \leq r \leq a + d, \theta) = 0 \quad (14)$$

and

$$c_M(t = 0, r \rightarrow \infty, \theta < \pi/2) = c_M^* \quad (15)$$

Equation 15 represents the initial introduction of M species in the medium far from the particle, as schematized in Figure 1. Because L and ML complex are only present within the shell (i.e.,  $c_{ML}(t,r > a + d,\theta) = 0$ ), eq 14 reflects accordingly the impossibility to form ML at  $t = 0$  within the soft component of the particle. The required spatial boundary conditions associated to eqs 12 and 13 and pertaining to M concentration within and outside the soft surface layer are detailed below.

$$\nabla c_M(t, r \rightarrow \infty, \theta) \rightarrow \vec{0} \quad (16)$$

which translates bulk condition for free metal species. For dilute suspensions of soft ligand particles as examined here (section 2.1), eq 16 is equivalent to setting  $c_M(t,r \rightarrow \infty,\theta) \rightarrow c_M^*$ . Denoting

as  $\vec{J}_M(t, r, \theta) = -D_{M,\text{in/out}} \nabla c_M(t, r, \theta) + \bar{u} c_M(t, r, \theta)$  the local flux of metal M inside the shell or outside the particle, we further have

$$\vec{J}_M(t, r, \theta) \cdot \vec{n}|_{r=a} = 0 \quad (17)$$

where  $\vec{n}$  is the unitary vector normal to the core particle. Equation 17 originates from the impermeability of the core particle component to ions and flow. Finally, the continuity of the metal flux and metal concentration at the position ( $r = a + d, \theta$ ) necessarily requires

$$\vec{J}_M(t, r = \{a + d\}^+, \theta) = \vec{J}_M(t, r = \{a + d\}^-, \theta) \quad (18)$$

and

$$c_M(t, r = \{a + d\}^+, \theta) = c_M(t, r = \{a + d\}^-, \theta) \quad (19)$$

**2.4. Effective Kinetic Rate Constants  $k_{a,d}^*$ , Dynamic Criteria for Colloidal Complex.** As extensively discussed in refs 6, 7, 9, 10, the dynamic criterion for colloidal metal complex resulting from the interaction between M and particle-confined ligands L should be evaluated by replacing the complex association–dissociation rate constants  $k_{a,d}$ , valid for homogeneous ligand solution, by their colloidal equivalents  $k_{a,d}^*$ . The latter involve contributions from reaction kinetics in the shell and diffusion/convection metal transport within and outside the particle. For dynamic ML colloidal complex, the effective rates  $k_{a,d}^*$  are fast on the experimental time scale  $t$  thus yielding

$$k_d^* t, k_a^* \rho_L^V t \gg 1 \quad (20)$$

The other limit given by  $k_d^* t, k_a^* \rho_L^V t \ll 1$  refers to static or inert ML complexes. Basically, within the given time scale  $t$ , dynamic complexes are able to restore equilibrium between M and L while static complexes do not. They respectively correspond to fast and slow rates for the volume complexation reactions.<sup>16</sup> It is beyond the scope of this paper to further comment on the above criteria. For complete details, the reader should refer to the seminal paper by Pinheiro et al.<sup>6</sup> as well as to the two first publications of this series<sup>9,10</sup> where a complete background of eq 20 may be found. The quantity  $\rho_L^V$  is defined as the ligand concentration over the whole solution volume and is related to the local concentration  $c_L^*$  of ligands within the shell,<sup>9,10</sup> that is,

$$\rho_L^V = \frac{4\pi}{V_c} \int_a^{a+d} r^2 c_L dr = \frac{V_c c_L^*}{V_c} \quad (21)$$

with  $V_s$  the volume of the shell layer. In eq 21,  $V_c$  is the volume of a spherical cell which encompasses the particle, with this volume being inferred from a Kuwabara cell model representation of the soft ligand particle suspension, as extensively discussed in the previous papers of this series.<sup>9,10</sup> In details, the radius of this cell, denoted as  $r_c$  (Figure 1), is related to the particle number concentration  $c_p$  and particle volume fraction  $\phi$  according to  $r_c = (a + d)\phi^{-1/3} - a = (4\pi c_p/3)^{-1/3} - a$  and  $r_c > a + d$  for dilute particle suspensions.<sup>9,10</sup> The effective rates

$k_{a,d}^*$  for the formation/dissociation of colloidal complex satisfy the conservation equation written at the scale of the cell<sup>9,10</sup>

$$\frac{\partial \rho_{i=M,ML}^V(t)}{\partial t} = \pm \{ k_d^* \rho_{ML}^V(t) - k_a^* \rho_M^V(t) \rho_L^V \} \quad (22)$$

where  $\rho_{i=M,ML}^V(t) = (2\pi/V_c) \int_a^{a+r_c} r_0^2 r^2 c_i(t, r, \theta) \sin \theta dr d\theta$  is the concentration of M and ML over the whole cell volume and is depending on the local concentrations  $c_i$ . The + sign in eq 22 holds for  $i = M$  and the – sign is for  $i = ML$ . Following rigorously the strategy adopted in ref 9, it may be shown that the searched  $k_a^*$  is depending on time  $t$  and local rate constant  $k_a$  according to

$$\frac{k_a^*(t)}{k_a} = \frac{\rho_M^S(t) \rho_L^V - \rho_{ML}^V(t) K^{-1}}{\rho_M^V(t) \rho_L^V - \rho_{ML}^V(t) K^{-1}} \quad (23)$$

where the volume concentration of free metal within the shell layer at time  $t$ , denoted as  $\rho_M^S(t)$ , is defined according to  $\rho_M^S(t) = (2\pi/V_s) \int_a^{a+d} r_0^2 r^2 c_M(t, r, \theta) \sin \theta dr d\theta$ . In eq 23,  $K$  is the ML stability constant defined by  $K = k_a/k_d$ .

**2.5. Computation Procedure for  $k_{a,d}^*$ , Derivation of Approximate Analytical Expression. Numerical Procedure.** The set of partial differential eqs 2, 3, and 11–13 and accompanied boundary conditions 4–10, 14–19 rigorously define the time-dependence of the spatial distributions for the M and ML concentrations within (for ML and M) and outside (for M) the particle colloidal shell. The equations were solved using numerical codes developed with Comsol Multiphysics (version 3.4, Consol AB, Sweden) and written for the sake of convenience in axial-symmetric cylindrical geometry (computation done in a large cylindrical domain enclosing a single soft ligand particle; see further details in Supporting Information, Figure S1). In particular, the nonlinear steady-state hydrodynamic problem was solved using an affined invariant form of the damped Newton method<sup>32</sup> applied to the discretized equivalent of the equations appropriately linearized according to linearization point strategy. The nonlinear dynamic differential equations pertaining to M/ML concentration polarizations were discretized following the method of lines and subsequently solved using differential algebraic equations solver developed in ref 33 and based on implicit time-stepping scheme. The governing equations were discretized on a nonuniform mesh grid with a large density of elements close to the particle surface and within the reactive shell. Once  $c_{M,ML}(t, r, \theta)$  was fully determined, the concentrations  $\rho_{i=M,ML}^V(t)$  and  $\rho_M^S(t)$  defined in section 2.4 could be evaluated by appropriate volume integration. Following this, the ratio  $k_a^*(t)/k_a$ , given by eq 23, may be estimated as a function of particle geometry (parameters  $a$  and  $d$ ), hydrodynamic penetration length  $1/\lambda_o$ , and Péclet number  $Pe$ . Additionally, the steady-state regime where the ratio  $k_a^*(t)/k_a$  reaches a time-independent constant value could be clearly identified. As recalled below and discussed in our previous studies,<sup>9,10</sup> this regime corresponds to the nonequilibrium chemical regime. Within the framework of this study, special attention will be devoted to analyze the dependence of  $k_a^*$  on  $a$ ,  $d$ ,  $1/\lambda_o$ , and  $Pe$  in the steady-state time window. We systematically verified that the obtained numerical solutions for  $c_{M,ML}(t, r, \theta)$  and  $\bar{u}(r, \theta)$  were independent of the size/local density of the chosen mesh and size of the simulation box. Additionally, solution of the hydrodynamic problem for  $Re \ll 1$  (the convective acceleration term in eq 3 may then be neglected) were successfully compared

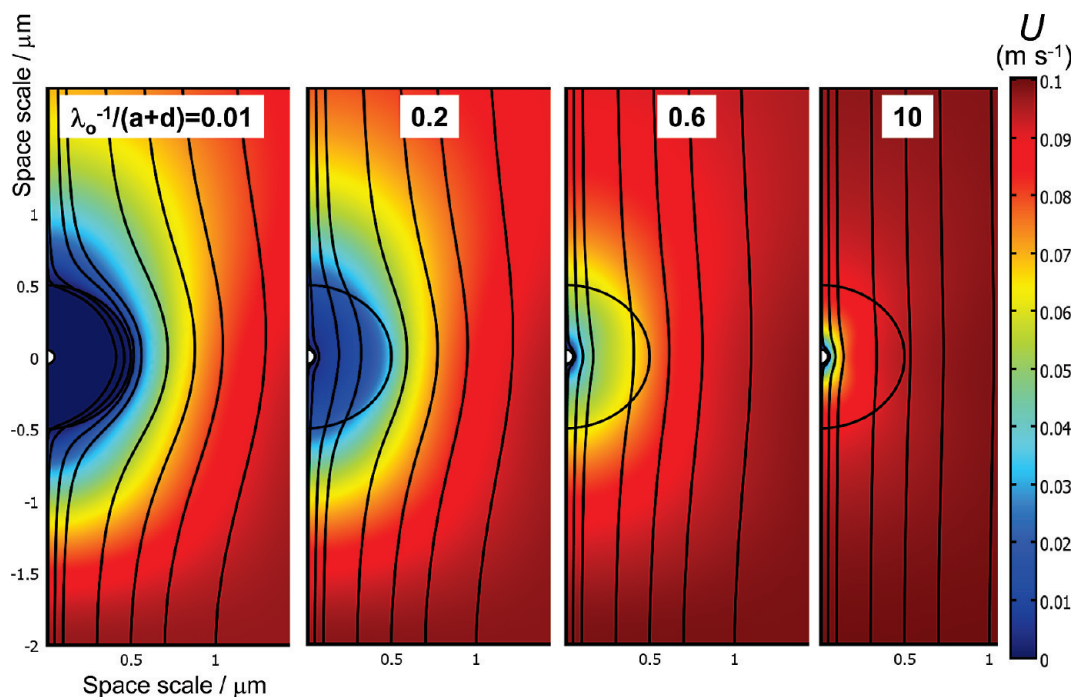


**Figure 2.** Contour surfaces for the velocity field and streamlines within and outside a colloidal ligand particle for  $a = 50 \text{ nm}$ ,  $d = 450 \text{ nm}$ ,  $U_0 = 0.1 \text{ m s}^{-1}$ , and various hydrodynamic penetration lengths  $\lambda_o^{-1}$  (indicated). Because of symmetry of the problem with respect to the axes  $\theta = 0$  and  $\theta = \pi$ , only half of the particle is represented. The  $x-y$  scales are given in  $\mu\text{m}$ .

to those obtained from the analytical solution detailed in Supporting Information. As further commented in section 3, the consistency of the numerical results was further confirmed by successful comparison of the ratio  $k_a^*(t)/k_a$ , evaluated in the steady-state regime under conditions of insignificant particle hydrodynamic permeability ( $1/\lambda_o \ll 1$ ) and purely diffusion-controlled metal mass transfer ( $Pe \ll 1$ ), with predictions based on the analytical formulation reported in ref 9 and valid for diffusive metal transport to and from the reactive shell (eq 24 below).

**Analytical Formulation.** In a situation where diffusion is the only relevant transport mode for the free metal species M, it was previously demonstrated<sup>9</sup> that the complex association rate constant  $k_a^*$  may be satisfactorily approximated in the steady-state nonequilibrium chemical regime by

$$k_a^*/k_a = \left( 1 + \frac{k_a \rho_L^V}{4\pi(a + d)D_M c_p} \right)^{-1} \quad (24)$$

which holds for dilute suspensions of soft particles. The approximations leading to eq 24 are essentially the neglect of M and ML concentration polarizations within the shell layer and the neglect of the interphasial electric field across the soft interphase. The latter approximation is relaxed in ref 10 where correction of eq 24 for metal conduction transport is explicitly worked out.

For sufficiently large Péclet number  $Pe \gg 1$  and thin layer shell  $d \ll a$ , the free metal concentration can be taken as constant within the shell; that is, we may neglect therein the angular and radial polarizations of M (and ML) concentration(s). For such situations, making use of the well-known Levich expression for diffusional flux of an ion to an impermeable, hard particle surface under conditions  $Pe \gg 1$  and  $Re \ll 1$  (see ref 34 and Supporting Information), we show that, in the

steady-state nonequilibrium chemical regime,  $k_a^*$  is given by the expression

$$k_a^*/k_a = \left( 1 + \frac{k_a \rho_L^V}{\frac{(3\pi)^{5/3}}{2\Gamma(1/3)}(a + d)^{4/3}c_p D_M^{2/3} U_0^{1/3}} \right)^{-1} \quad (25)$$

For full details on the derivation of eq 25, the reader should refer to Supporting Information. In deriving eq 25, diffusion coefficients of metal M are taken identical within and outside the shell  $D_M = D_{M,\text{in}} = D_{M,\text{out}}$ , and  $\Gamma$  is the gamma function. The denominator which involves particle size, diffusion coefficient, and bulk liquid velocity corresponds physically to the total rate of metal mass transfer to the hard ligand particle. In particular, the power-dependence of this quantity on  $D_M$  is characteristic of convective-diffusion controlled transport. The authors experienced that explicit account of flow penetration within the shell layer ( $1/\lambda_o > 0$ ) and/or of angular M concentration polarization ( $Pe \sim 1$ ) renders impossible any tractable, analytical derivations of  $k_a^*$ . These cases are handled by the numerical formalism detailed above and valid for any values of  $Pe$  and  $1/\lambda_o$ , providing laminar flow conditions remain satisfied (see section 2.1). In line with this, no simple, explicit universal scaling of the dependence of  $k_a^*$  on  $Pe$  and  $1/\lambda_o$  may be performed for the general situation of metal speciation in permeable ligand particle shell.

### 3. Results and Discussions

**3.1. Impacts of Flow Field on the M/ML Concentration Profiles and on  $k_a^*/k_a$  in the Steady-State Nonequilibrium Chemical Regime. Fluid Flow Dynamics.** As a starting point, we give in Figure 2 the steady-state hydrodynamic flow field profile around and within the colloidal ligand particle for various hydrodynamic penetration lengths  $1/\lambda_o$ . To exemplify the flow

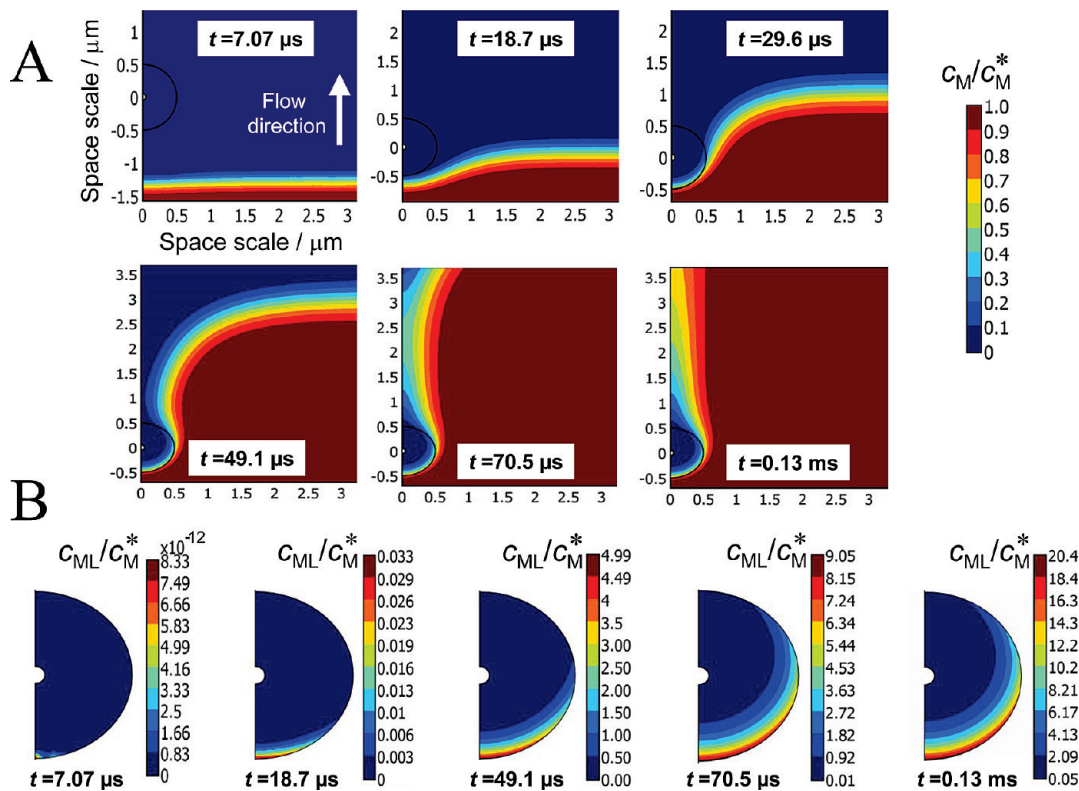


**Figure 3.** M (panel A) and ML (panel B) concentration contour surfaces as a function of time (indicated) for  $\lambda_o^{-1} = (a + d)/5$ . Other model parameters:  $a = 50 \text{ nm}$ ,  $d = 450 \text{ nm}$ ,  $U_o = 0.1 \text{ m s}^{-1}$ ,  $D_M = D_{M,\text{in}} = D_{M,\text{out}} = 10^{-9} \text{ m}^2 \text{s}^{-1}$ ,  $c_M^* = 10^{-2} \text{ mol m}^{-3}$ ,  $\rho_L^Y = 3.7 \times 10^{-6} \text{ mol m}^{-3}$ ,  $T = 298 \text{ K}$ ,  $K = 5 \times 10^4 \text{ mol}^{-1} \text{ m}^3$ ,  $k_a = K_{\text{os}} k_w^{14-16}$  with  $k_w = 7 \times 10^9 \text{ s}^{-1}$ ,  $K_{\text{os}} = 3.66 \times 10^{-3} \text{ mol}^{-1} \text{ m}^3$ . The values of  $D_M$  and  $k_w$  pertain to Pb(II) metal ion (ionic strength 0.01 M) while that of  $K$  is typical of metal complexation by carboxylate groups distributed at the surface of latex particles.<sup>6</sup> The value of  $\rho_L^Y$  considered is in agreement with the condition  $r_c >> a + d$ . In panel A, the  $x-y$  scales are given in  $\mu\text{m}$ .

pattern, the particle is taken as nearly porous with a radius  $a = 50 \text{ nm}$  and  $a/(a + d) = 0.1$ . Under conditions of Figure 2, the particle size and bulk fluid velocity correspond to  $Pe = 50$  and  $Re = 0.05$ . In line with predictions obtained from the analytical formulation of the hydrodynamic problem detailed in Supporting Information, the distortion of the streamlines from rectilinear profiles when passing around the particle are the most pronounced for impermeable shell ( $1/\lambda_o \ll d$ ) and become insignificant for sufficiently large  $1/\lambda_o$ , that is, when the shell gradually becomes free draining. The larger  $1/\lambda_o$  is, the more the approaching flow is able to enter the particle shell, or for that matter, the larger the fluid flow penetration. For small values of  $1/\lambda_o$ , the fluid tends to flow along the outer edge of the particle shell where it experiences a reduced friction. Accordingly, upon increase of  $1/\lambda_o$ , the magnitude of the local velocity field within the shell increases from zero for impermeable layer to bulk value  $U_o$  for  $1/\lambda_o > d$ . In all cases and under the condition  $Re \ll 1$ , the stream function exhibit a maximum for  $\theta = \pi/2$  (see Supporting Information) and so do the corresponding streamlines. The viscous retardation acts to decrease the flow velocity, and systematically, this retardation is the most important in the vicinity of the impermeable core particle surface where the no-slip condition prevails.

**Transitory Evolution of M/ML Concentration Distributions.** As detailed in section 2.3, metal species are introduced in the moving liquid at  $t = 0$ . Figure 3 depicts the typical concentration profiles obtained for M (within and around the shell, panel A) and ML (within the shell, panel B) as a function of time under the conditions of Figure 2 with  $\lambda_o^{-1} = (a + d)/5$ . In a first stage, that is, for  $t = 0^+$ , the front edge separating the spatial positions, where  $c_M = 0$  (downstream side) and  $c_M = c_M^*$  (upstream side), is flat, that is, oriented perpendicular to the axis  $\theta = 0$ . While

it maintains such a configuration, it progresses at the velocity  $U_o$ . Sufficiently far away from the right side of the particle, the flow field remains uniform (Figure 2), and the front edge there keeps on advancing with velocity  $U_o$  until metal concentration reaches bulk value  $c_M^*$ . In the vicinity of the particle, after some delay, M species significantly penetrate by convective-diffusion within the shell layer and react with the therein distributed ligands L; the formed complex ML then starts to appear at the pole  $\theta = 0$ . Accordingly,  $c_M$  and  $c_{ML}$  decrease from the outer edge of the particle to the very core/shell interface as a result of the differences in M chemical potential within and outside the particle.<sup>8</sup> The aforementioned front edge then starts to deform appreciably in both angular and radial dimensions as a result of the two-dimensional, transitory building of M diffusion layer across the shell and in solution. Upon further increase of time, ML concentration increases within the shell (see the scales in panel B, Figure 3) because of the ongoing reaction 1 and the ML species are progressively present deeper inside the shell. At fixed  $\theta$ , ML concentration gradient over the whole particle radius,  $[c_{ML}(t,r = a + d,\theta) - c_{ML}(t,r = a,\theta)]/(a + d)$ , increases with time and, for a given  $t$ , it is significantly reduced for increasing values of  $\theta$  with  $c_{ML}(t,a < r < a + d,\theta \sim \pi) = 0$ . The negligible contribution of the downstream side of the particle ( $\theta > \pi/2$ ) in the overall metal mass transfer (or equivalently in the overall ML complex formation) stems from the therein thicker diffusion layer thickness as compared with that developed in the upstream part ( $\theta < \pi/2$ ), a result pointed out by Levich for steady-state convective diffusion layers around hard particles.<sup>34</sup> For sufficiently long time (not shown in Figure 3), M and ML concentration gradients in the  $r$  and  $\theta$  directions within and/or outside the shell particle vanish; chemical equilibrium is then reached with the M and ML concentrations

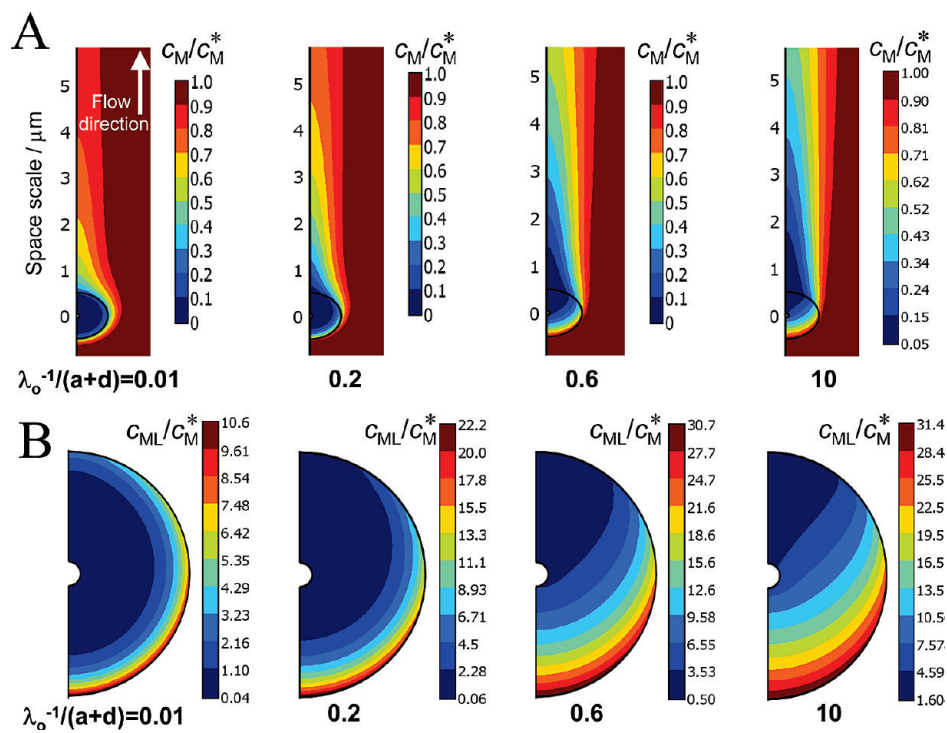


**Figure 4.** M (panel A) and ML (panel B) concentration contour surfaces in steady-state nonequilibrium chemical regime for various  $\lambda_o^{-1}$  (indicated). Other model parameters as in Figure 3. In panel A, the y scale is given in  $\mu\text{m}$ . For detailed M/ML concentration profiles at different  $\theta$  angles under conditions of Figure 4, see Figure S3 in Supporting Information.

satisfying locally the thermodynamic expression  $c_{\text{ML}}(t \rightarrow \infty, r, \theta)/c_{\text{M}}(t \rightarrow \infty, r, \theta)c_{\text{L}}^* = K$  and  $c_{\text{M}}(t \rightarrow \infty, r, \theta) \rightarrow c_{\text{M}}^*$ .<sup>9</sup>

While increasing the time  $t$  from 0 to  $t = \infty$  (thermodynamic equilibrium regime), M and ML concentration profiles pass through a (quasi) steady-state regime. The existence of this nonequilibrium chemical regime is analogous to that extensively commented in refs 9 and 10 where convective metal mass transport was ignored. This regime may be clearly identified upon inspection of the time dependence of  $k_a^*$ .<sup>9,10</sup> In Supporting Information (Figure S2), we provide  $k_a^*$  as a function of  $t$  for the situation depicted in Figure 3. The basic features of this curve are similar to those discussed at length in refs 9 and 10. The quasi steady-state regime corresponds to the time domain where  $\partial k_a^*/\partial t \sim 0$ ; that is, the  $\theta$ -dependent diffusion flux of free metal species at the shell/solution interface maintains its steady-state nature while time variation for the local M and ML concentrations are present (Supporting Information). In previous reports,<sup>9,10</sup> the denomination “quasi steady-state” for this regime was justified by arguing that the true steady-state actually corresponds to the thermodynamic regime where  $dc_{\text{M},\text{ML}}/dt = 0$ . In the following and for the sake of simplicity, we shall make the amalgam between “quasi steady-state” and “steady-state”, keeping in mind the difference given above. In Figure 3, the M and ML profiles depicted for  $t = 0.13$  ms fall in the aforementioned steady-state regime, as shown in Supporting Information. In the rest of the analysis, we shall focus on metal speciation dynamics within the steady-state regime because it pertains to the typical time window explored in speciation experiments, for example, by SSCP (stripping chronopotentiometry at scanned deposition potential<sup>6,7</sup>), where ligand particles are placed in a large-scale diffusion layer (of thickness much larger than the particle size) developed in the vicinity of a consuming interface (like an electrode or a microorganism).

### Steady-State M/ML Concentration Profiles: Effects of Fluid Flow.

Given the above motivation, Figure 4 displays the two-dimensional M (panel A) and ML (panel B) steady-state concentration contour surfaces under the conditions of Figure 2 as a function of the fluid flow penetration degree  $\lambda_o^{-1}$  for situations of impermeable ( $\lambda_o^{-1} < d$ ), partially permeable, and fully permeable ligand particles ( $\lambda_o^{-1} > d$ ). Under conditions of Figure 4, steady-state is reached after  $\sim 10^{-4}$  s, as shown in Figure S2 in Supporting Information. Refined graphical representations of the angular and radial dependences of  $c_{\text{M},\text{ML}}$  are further given in Supporting Information (Figure S3) which the reader should refer to. Overall, there is a clear connection between the flow field distributions depicted in Figure 2 and the distortion of the M/ML concentration contour surfaces upon increase of  $\lambda_o^{-1}$ . ML concentration contour surfaces basically follow the spherical geometry of the particle at low  $\lambda_o^{-1}$  while severe angular distortions, particularly in the downstream side of the particle, are observed upon increase of  $\lambda_o^{-1}$ . When increasing the degree of fluid flow penetration within the particle, the overall amount of ML species formed in the shell increases (see scales in panel B, Figure 4); ML concentration increases deeper inside the shell and gradually decreases within the downstream part of the ligand particle ( $\theta \sim \pi$ ). Qualitatively, with increasing  $\lambda_o^{-1}$ , similar features are observed for the M concentration contour surfaces within the shell layer. Outside the particle, these are strongly distorted in the downstream side of the particle ( $r > a + d, \theta > \pi/2$ ) as if they were blown by the flowing fluid. In details, inspection of the data given in Supporting Information reveals that, for a fixed radial position outside and/or within the shell layer,  $c_{\text{M},\text{ML}}(r, 0 < \theta < \pi/2)$  increase upon increase of  $\lambda_o^{-1}$  as a result of efficient convective-diffusion transfer of M from bulk medium to the permeable reactive shell, and subsequent complex formation. In the angular domain  $0 < \theta < \pi$ , for fixed  $\lambda_o^{-1}$  and for a given position  $r$  in the vicinity of/within the ligand particle,  $c_{\text{M}}$  and  $c_{\text{ML}}$  decrease

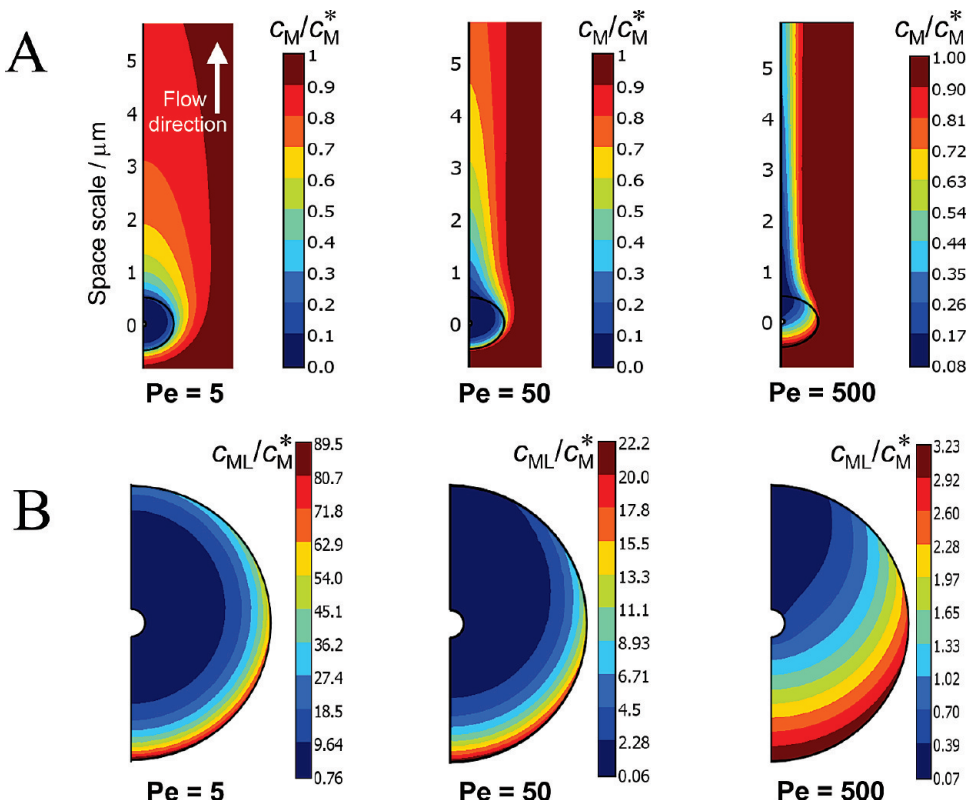


**Figure 5.** M (panel A) and ML (panel B) concentration contour surfaces in steady-state nonequilibrium chemical regime for various bulk flow velocity field  $U_o$  (or equivalently different values of the Péclet number  $Pe$ , indicated). Other model parameters as in Figure 3. In panel A, the y scale is given in  $\mu\text{m}$ . For detailed M/ML concentration profiles at different  $\theta$  angles under conditions of Figure 5, see Figure S4 in Supporting Information.

upon increase of  $\theta$ . This is explained by the corresponding increase of the M diffusion layer thickness (confirmed by inspection of the M concentration polarization domains) and the accompanied decrease in metal mass transfer to the particle. For impermeable particles ( $\lambda_o^{-1} < d$ ), radial diffusion of M within the reactive shell layer is not hindered by lateral convection so that, in this layer, M and ML concentration profiles are reminiscent of those obtained by considering spherical diffusion as the predominant transport mode.<sup>9</sup> For angular positions  $\theta \sim \pi$  and fixed position deep inside the shell (close to the core surface),  $c_{M,ML}$  increase with  $\lambda_o^{-1}$  for the reason mentioned previously. For positions  $r > a + d$ , however,  $c_M$  decreases with increasing  $\lambda_o^{-1}$ . These nonmonotonous variations of  $c_M$  across the shell/solution interphase stem from the blowing of the M species by the fluid flow and further account for the presence of maxima in the evolution of  $c_{ML}$  with  $\lambda_o^{-1}$  at fixed radial position  $r = (a + d)^-$ .

For the sake of completeness, we give in Figure 5 the typical M and ML concentration contour surfaces under the conditions specified in Figure 4 for  $\lambda_o^{-1} = (a + d)/5$  and various bulk fluid flow velocity  $U_o$ , or equivalently various Péclet number  $Pe$ . The corresponding detailed M and ML concentration profiles are provided in Supporting Information (Figure S4) while Figure S2 therein indicates that steady-state conditions are reached after  $\sim 10^{-5}$  s,  $10^{-4}$  s, and  $10^{-3}$  s for  $Pe = 500$ , 50, and 5, respectively. It is worth recalling that the situation  $Pe = 0$  corresponds to that of pure diffusion-controlled M transport as analyzed in details in ref 9. Accordingly, the angular polarizations for the M and ML concentrations are the least significant for low  $Pe$ , in agreement with results of Figure 5. Additionally, for low  $Pe$ , the M concentration contour surfaces exhibit an ovoid shape elongated toward the downstream side. When increasing  $Pe$ , the spatial area covered by this ovoid strongly

decreases, and its tail in the downstream side gets gradually parallel to the axis  $\theta = \pi$ . This feature is correlated to the decrease for a fixed angle  $\theta$  of the diffusion layer thickness upon increase of the flow velocity  $U_o$ , as shown by Levich<sup>34</sup> for hard, impermeable particles. Qualitatively, the dependences of M concentration profile on  $Pe$  within and in the close vicinity of the ligand particle are strictly analogous to those commented in Figure 4 when analyzing the effect of  $\lambda_o^{-1}$ . The free metal mass transfer toward the particle is indeed optimized either upon reduction of the friction exerted on the flow within the shell (i.e., increase of  $\lambda_o^{-1}$ ) or upon increase of the flow velocity. For the complex ML, the situation is somewhat different. Upon increase of  $Pe$  and regardless of the magnitudes of the contour ML concentration surfaces, the radial and angular distributions of the latter remain very similar to those commented in Figure 4B. However, the total amount of ML species formed within the shell now decreases drastically with increasing  $Pe$  while it increased with increasing  $\lambda_o^{-1}$  (see Figure 4B). This is explained by the fact that the lateral flow developed along the particle (Figure 2) tends to expel rapidly the free metal species from the reacting shell before they have a chance to diffuse toward the particle and react with L. Said differently, increasing  $U_o$  comes to decrease the residence time of M within the shell layer. In the event that this residence time is much smaller than the time required for association of M with L, convection then renders inoperative the formation of ML complex. Such situation is favored with increasing  $U_o$  (or  $Pe$ ), so that in turn  $c_{ML}$  basically decreases in the shell and ultimately goes to zero for  $Pe >> 1$ .

**Effects of Fluid Flow on Speciation Dynamics ( $k_a^*$ ) in Steady-State.** Following the above analysis of the M and ML concentration polarization features as a function of  $Pe$  and  $\lambda_o^{-1}$ , we are now ready to examine the dependences of  $k_a^*$  (in the

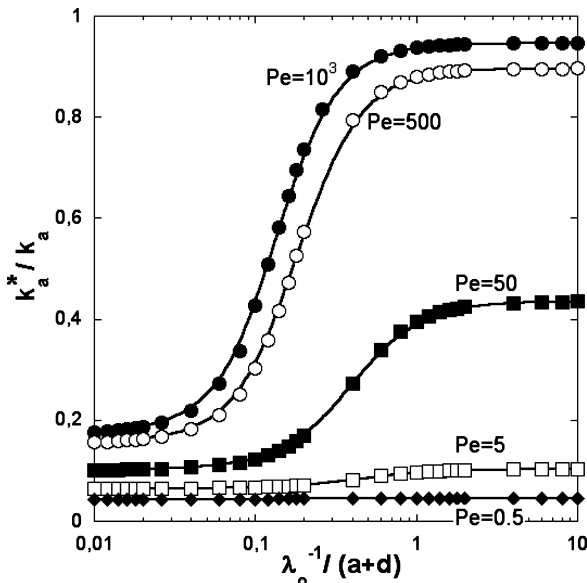


**Figure 6.** Dependence of the ratio  $k_a^*/k_a$  on  $U_o$  (or  $Pe$ , indicated) and  $\lambda_o^{-1}$  in the steady-state nonequilibrium chemical regime. Plain lines are only guides to the eye, and symbols represent the numerical results. Model parameters as in Figure 3.

nonequilibrium steady state regime) on  $Pe$  (i.e.  $U_o$ ) and  $\lambda_o^{-1}$  (Figure 6), the particle geometry being that adopted in Figures 2–5. From Figure 6, it is clear that the effective formation rate constant of the complex ML,  $k_a^*$ , may significantly differ from  $k_a$  depending on the particle permeability and flow field magnitude. This comes to state that the dynamic properties of the colloidal complex (eq 20) within the nonequilibrium steady-state time window are inherently depending on the flow field structure within and outside the shell. First, we note that  $k_a^*/k_a$  is independent of  $\lambda_o^{-1}$  for  $Pe \rightarrow 0$ . The latter situation is that where M transfer from/toward the shell is solely ensured by diffusion transport, that is, the nature of the flow field, in particular its degree of penetration within the shell, does not play any role in governing M/ML concentration distributions. It is further verified that the corresponding  $k_a^*/k_a$  value is in excellent agreement with that derived from eq 24. For this situation where  $k_a^*/k_a < 1$ , metal speciation is rate-limited by diffusion transport of free metal ions to and from the soft surface layer that contains the binding sites. For  $Pe > 1$ ,  $k_a^*/k_a$  increases with  $\lambda_o^{-1}$  following a sigmoid curve: the asymptotic values reached at very low and very large  $\lambda_o^{-1}$  pertain to the limiting cases of impermeable and entirely free draining reactive layers, respectively. For a given  $\lambda_o^{-1}$ ,  $k_a^*/k_a$  increases upon increase of  $Pe$ , and this increase is the most significant for large particle permeability. These results indicate that introduction of finite flow within the shell and/or increase of fluid velocity within/outside the particle improve the efficiency for transferring free metals toward the particle shell (Figure 4). In doing so, the contribution of kinetics ( $k_{a,d}$  molecular constants) in ML complex formation becomes increasingly important in determining the dynamics of the overall speciation process. For  $k_a^*/k_a$  approaching unity, as met at sufficiently large  $\lambda_o^{-1}$  and high  $Pe$ , the rate of reaction 1 is solely determined by the kinetics of interconversion of M into ML. For intermediate values of  $k_a^*/k_a$  between 0 and 1, that is, for partially permeable particles, coupling between the kinetic determinants of reaction 1 and the convective-diffusion transport of free metal to and from the soft surface layer come into play. The above effects are further in line with the M/ML profiles commented in Figure 4. Indeed, in the angular region that counts most in determining the overall M

mass transfer ( $0 < \theta < \pi/2$ ) to the particle, the shell is significantly filled with free metal species upon increase of  $\lambda_o^{-1}$  and/or  $Pe$ ; the flux of metal over the whole particle then increases, and in turn the local kinetic interconversion of M into ML within the shell becomes gradually rate-limiting. In the light of Figure 6 and referring to the definition of the dynamic criterion given by eq 20, we conclude this section by stating that, under flow conditions, colloidal complexes ML are more static for ligand particles characterized by reduced hydrodynamic permeability and more dynamic when formed in media defined by high Péclet numbers. These fundamental results are of primary importance when investigating speciation dynamics, for example, in porous aggregates of ligand particles under flow.

**3.2. Impacts of Soft Particle Size on the Dependences of  $k_a^*/k_a$  on  $Pe$  and  $\lambda_o^{-1}$  in Nonequilibrium Steady-State Regime.** In Figure 7, the effects of the particle size  $a + d$  on the dynamic properties of the colloidal complex ML are analyzed as a function of  $\lambda_o^{-1}$  for  $U_o = 1$  (panel A),  $10^{-1}$  (B),  $10^{-2}$  (C), and  $10^{-3} \text{ m s}^{-1}$  (D). In all cases, the particle remains nearly porous with  $a/a + d = 0.1$ , and for the sake of comparison, the ligand concentration throughout the solution,  $\rho_L^V$ , is maintained constant by adequate dimensioning of the simulation box. For a fixed particle size, the dependences of  $k_a^*/k_a$  with  $\lambda_o^{-1}$  and  $U_o$  are in line with those discussed in Figure 6. In particular, for  $Pe \rightarrow 0$  (panel D), the ratio  $k_a^*/k_a$  is independent of  $\lambda_o^{-1}$  and is in excellent agreement with prediction from eq 24. For fixed  $U_o$  and  $\lambda_o^{-1}$ ,  $k_a^*/k_a$  decreases upon increase of the particle size. The speciation process is then increasingly rate-limited by the diffusion transport of free metal from/toward the particle-confined ligands in the reactive shell; that is, the radial diffusional flux of M decreases and the formed colloidal complex ML then becomes more inert. Upon comparison with Figure 6, it is noted that increasing the Péclet number via increasing the particle size at fixed  $U_o$  and increasing  $U_o$  at constant size lead to opposite variations of  $k_a^*/k_a$ . Beyond the reasons given above for such behavior, the major difference in these two operations stems from the resulting impact on M radial diffusional flux at the outer edge of the particle. According to the derivation done in Supporting Information, this flux is proportional to the quantity  $U_o^{1/3}(a + d)^{-2/3}$ ,<sup>34</sup> thus confirming the dependence of the dynamic properties of ML complex on fluid velocity  $U_o$  and size  $a + d$ , as examined in Figures 6 and 7, respectively. We provide in Figure 7 the results obtained for  $k_a^*/k_a$  using eq 25 derived for hard, impermeable particles (i.e., for  $d \ll a$  and  $\lambda_o^{-1} \ll d$ ) in the limits  $Pe \gg 1$  and  $Re \ll 1$ . Overall, by comparing the  $k_a^*/k_a$  results of panels B–D with those estimated from eq 25, it is verified that the adequacy between the two, in the limit of reduced intraparticle flow penetration, is basically improved upon increase of the size and/or increase of  $U_o$ , that is, with increasing  $Pe$ . This is in agreement with the set of approximations underlying the validity of eq 25. In panel B where  $10 < Pe < 100$  and  $10^{-2} < Re < 10^{-1}$ , merging between the analytical and the numerical approaches is excellent to very satisfactory for all particle sizes investigated. The success of eq 25 in reproducing appropriately  $k_a^*/k_a$  for the porous particles of Figure 7 in the limit  $\lambda_o^{-1}/d \ll 1$  may however be paradoxal in view of the strict validity of eq 25 for  $d \ll a$ . This paradox was already discussed in ref 8 for the situation where diffusion solely governs M transport to the particle. The reason is that deriving eq 24 (diffusion transport) or eq 25 (convective-diffusion transport) with averaging  $c_{M,ML}$  within the shell and evaluating the M diffusional flux at the outer edge of the particle as if the latter is entirely hard (i.e.,

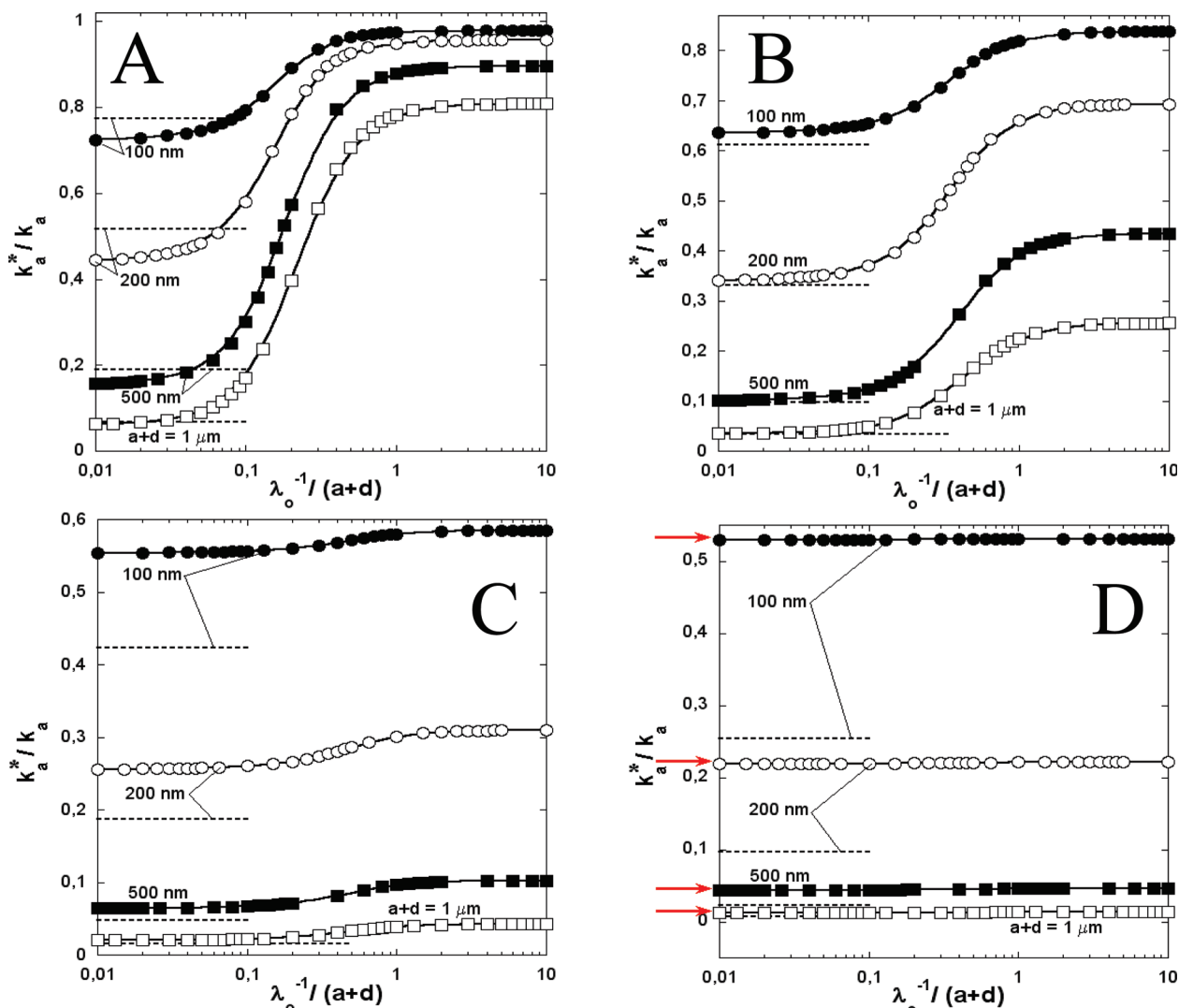


**Figure 7.** Dependence of the ratio  $k_a^*/k_a$  on  $\lambda_o^{-1}$  and particle size  $a + d$  (indicated) with  $d/(a + d) = 0.9$  (steady-state nonequilibrium chemical regime).  $U_o = 1$  (A), 0.1 (B),  $10^{-2}$  (C), and  $10^{-3} \text{ m s}^{-1}$  (D). Plain lines are only guides to the eye, and symbols represent the numerical results. Other model parameters as in Figure 3. The arrows in panel D are predictions from eq 24 while dotted lines pertain to  $k_a^*/k_a$  values obtained in the impermeable limit using eq 25.

with replacing  $a$  by  $a + d$  in the flux expressions) does not lead to major misevaluation of  $k_a^*/k_a$ . However, for very high flow velocity (panel A), the analytical results, while remaining acceptable, tend to slightly overestimate (by a few percent) the numerical estimations. Because  $k_a^*/k_a$  is necessarily bounded in the interval [0;1], the above overestimations are most striking for cases where the ratio  $k_a^*/k_a$  lies in the intermediate range  $\sim 0.2 - 0.8$ . Under conditions of high flow velocity  $U_o$ , significant M concentration changes deep inside the particle (Figure 5) are obtained so that, in turn, the diffusion flux expression for hard particles, modified upon replacing  $a$  by  $a + d$  therein, become less adapted.

**3.3. Impacts of the Core-to-Particle Size Ratio on the Dependences of  $k_a^*/k_a$  on  $Pe$  and  $\lambda_o^{-1}$  in Nonequilibrium Steady-State Regime.** In Figure 8,  $k_a^*/k_a$  is set against  $\lambda_o^{-1}$  for  $U_o = 1$  (panel A),  $10^{-1}$  (B), and  $10^{-2} \text{ m s}^{-1}$  (C), and attention is now devoted to analysis of the impact of the ratio  $a/(a + d)$  on the dynamic properties of the ML colloidal complex with fixed size  $a + d$  ( $= 500 \text{ nm}$ ). As done in the preceding sections, the quantity  $\rho_L^V$  is maintained constant upon adequate sizing of the simulation box, and results are depicted as a function of the dimensionless flow penetration length  $\lambda_o^{-1}/(a + d)$ . For a given particle geometry, the dependences of  $k_a^*/k_a$  on  $\lambda_o^{-1}$  and

fluid velocity  $U_o$  follow the trends discussed in Figure 6 and Figure 7. In the limit  $\lambda_o^{-1} \rightarrow 0$ ,  $k_a^*/k_a$  asymptotically approaches a constant value, and in Figure 8, this limit is only apparent since decrease of  $\lambda_o^{-1}/(a + d)$  below the value 0.01 generates further decrease of the ratio  $k_a^*/k_a$ . At fixed  $U_o$ , the inflection point of the sigmoid curve marking the variation of  $k_a^*/k_a$  with  $\lambda_o^{-1}$  is shifted to the left upon increase of  $a/(a + d)$ . Indeed, at fixed size  $a + d$ , such an increase goes in pair with a decrease of the shell thickness  $d$ , and with a shift of the impermeable and free draining limits (given by  $\lambda_o^{-1}/d << 1$  and  $\lambda_o^{-1}/d > > 1$ , respectively), to lower  $\lambda_o^{-1}$ . In the limit of impermeable particle shell,  $k_a^*/k_a$  increases upon increase of  $a/(a + d)$ , or equivalently, colloidal complex becomes more dynamic; that is, metal speciation is increasingly rate-limited by kinetics of M–ML interconversion. This is so because M–ML concentration polarizations within the shell are significantly reduced for an impermeable hard particle ( $d/a << 1$ ) as compared to the situation of impermeable porous particle. In the limit  $\lambda_o^{-1} < < d$  and for a given  $a/(a + d)$ , the larger  $U_o$ , the better  $k_a^*/k_a$  is approximated by eq 25, in agreement with the set of conditions underlying validity of this equation. More interestingly, for sufficiently large fluid flow velocity within the particle shell (i.e., sufficiently large  $\lambda_o^{-1}$  and/or  $U_o$ ), the ratio  $k_a^*/k_a$  first

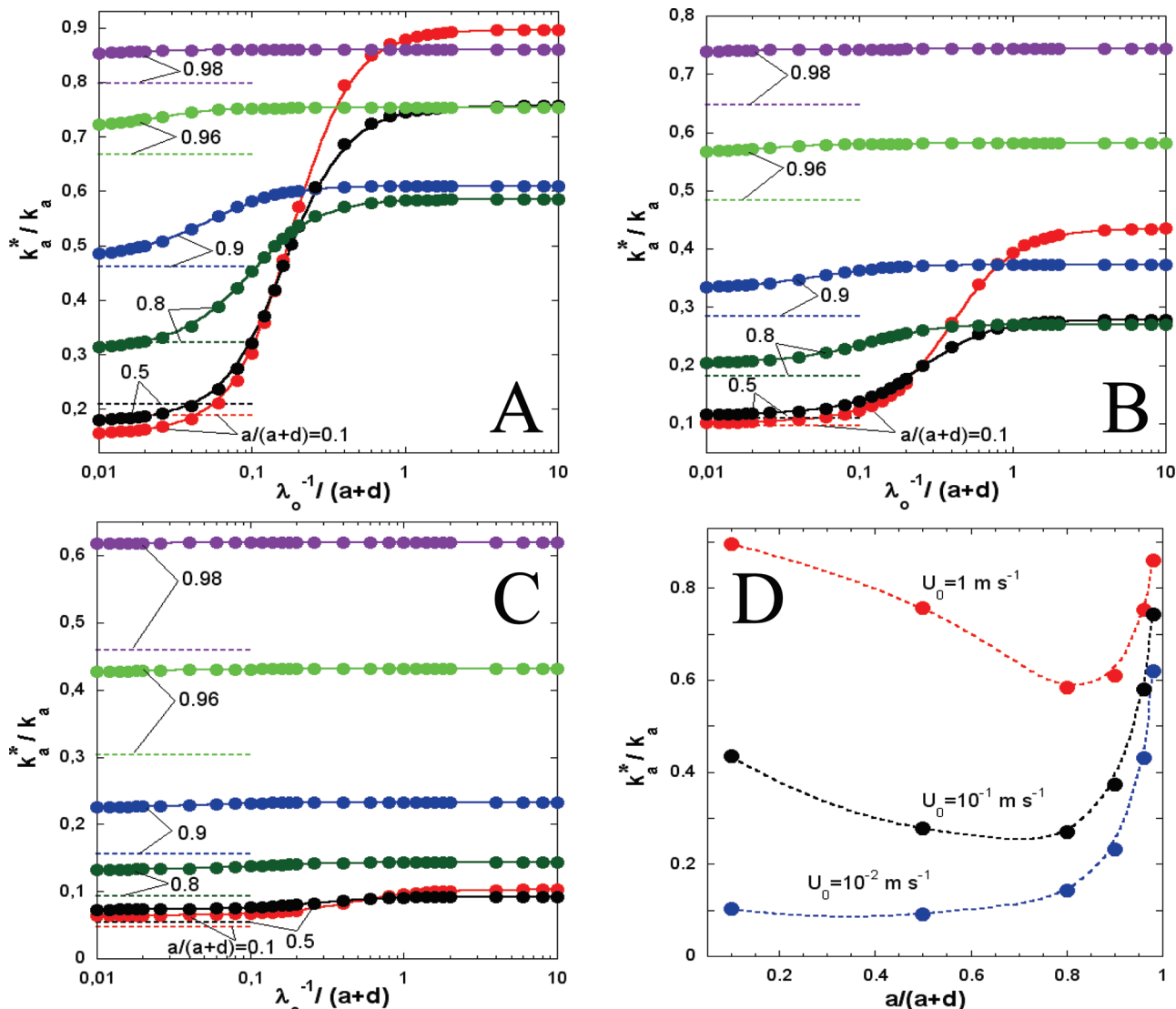


**Figure 8.** Dependence of the ratio  $k_a^*/k_a$  on  $\lambda_o^{-1}$  and core-to-particle size ratio  $a/(a+d)$  (indicated) with  $a + d = 500 \text{ nm}$  (steady-state nonequilibrium chemical regime).  $U_0 = 1$  (A), 0.1 (B), and  $10^{-2} \text{ m s}^{-1}$  (C). Plain lines are only guides to the eye, and symbols represent the numerical results. In panel D, representation of  $k_a^*/k_a$  as a function of  $a/(a+d)$  in the limit of free draining particle shell under conditions of panels A, B, and C. Other model parameters as in Figure 3. The dotted lines in panels A, B, and C pertain to  $k_a^*/k_a$  values obtained in the impermeable limit using eq 25.

decreases with increasing  $a/(a+d)$ , passes through a minimum, and then increases (panel D). The presence of this minimum, reached for  $a/(a+d) = \{a/(a+d)\}^*$ , is the result of the internal fluid flow structure modifications upon reduction of the shell thickness. Upon increase of the core radius at constant particle size, the flow becomes similar to a Stokes flow, and the metal ions are then able to reach the back of the particles which otherwise they could not reach. In more details, for  $a/(a+d) < \{a/(a+d)\}^*$ , the decrease of  $k_a^*/k_a$  with increasing  $a/(a+d)$  stems from the corresponding reduction of the fluid flow velocity within the shell, as illustrated in Figure 9. This in turn leads to a speciation process that is increasingly rate-limited by (radial) diffusion transport of free metal ions to and from the soft surface layer: the colloidal complex ML becomes more inert. From the threshold value  $\{a/(a+d)\}^*$ , further increases of  $a/(a+d)$  are accompanied by severe reduction of the M and ML concentration polarizations within the shell layer; the particle gradually turns into a hard type, and the physical origin for the corresponding increase of  $k_a^*/k_a$  is similar to that evoked above in the limit  $\lambda_o^{-1} \ll d$ . Conformably to expectation, the minimum in  $k_a^*/k_a$  becomes more shallow for decreasing values of  $U_0$  and

disappears in the diffusion limit  $Pe \rightarrow 0$  where  $k_a^*/k_a$  becomes independent of  $\lambda_o^{-1}$ .

**3.4. Effect of M Diffusion Coefficient and Eigen Kinetic Rate Constants on  $k_a^*/k_a$ .** Depending on the charge and steric compactness of the porous part of the soft particle, the diffusion coefficient  $D_{M,\text{in}}$  of free metals M within the shell may be lower than  $D_{M,\text{out}}$ .<sup>31</sup> Also, the nature of the metal impacts the magnitude of the kinetic rate constant  $k_a$ .<sup>15</sup> For the sake of completeness, the dependences of  $k_a^*/k_a$  on the ratio  $\varepsilon = D_{M,\text{in}}/D_{M,\text{out}}$  and on  $k_a$  are given in Figure 10A,B, respectively. The values chosen for the constant  $k_a = K_{\text{os}}k_w$  pertain to metals (Pb, Cd, Mn, Ni) characterized by similar  $K_{\text{os}}$  stability constant but very distinct rate constants  $k_w$  for water removal as defined within Eigen mechanism.<sup>14–16</sup> Results indicate that, for a given  $\lambda_o^{-1}$ ,  $k_a^*/k_a$  decreases upon decrease of  $\varepsilon$ . This agrees with the corresponding decrease of M diffusional flux: the process is then rate-limited by M diffusion transport, and ML colloidal complex becomes more inert. As expected, the effect of  $\varepsilon$  on speciation dynamics is strongly reduced for sufficiently large  $\lambda_o^{-1}$  and  $U_0$ , that is, when M–ML interconversion kinetics within the shell starts to critically limit the speciation process. For fixed hydrodynamic

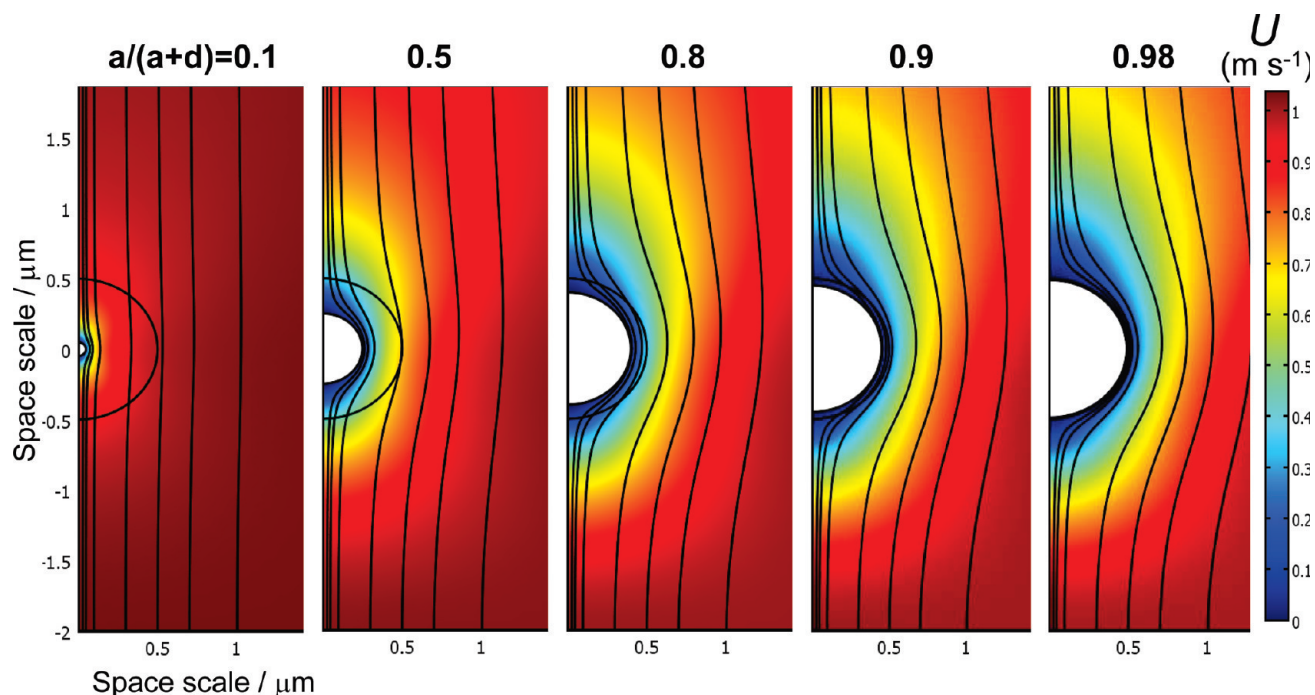


**Figure 9.** Contour surfaces for the velocity field and streamlines within and outside a colloidal ligand particle for various ratios  $a/(a + d)$  (indicated) and  $a + d = 500 \text{ nm}$ ,  $U_0 = 1 \text{ m s}^{-1}$ ,  $\lambda_o^{-1} = 10(a + d)$  (limit of free draining shell). The  $x$ - $y$  scales are given in  $\mu\text{m}$ .

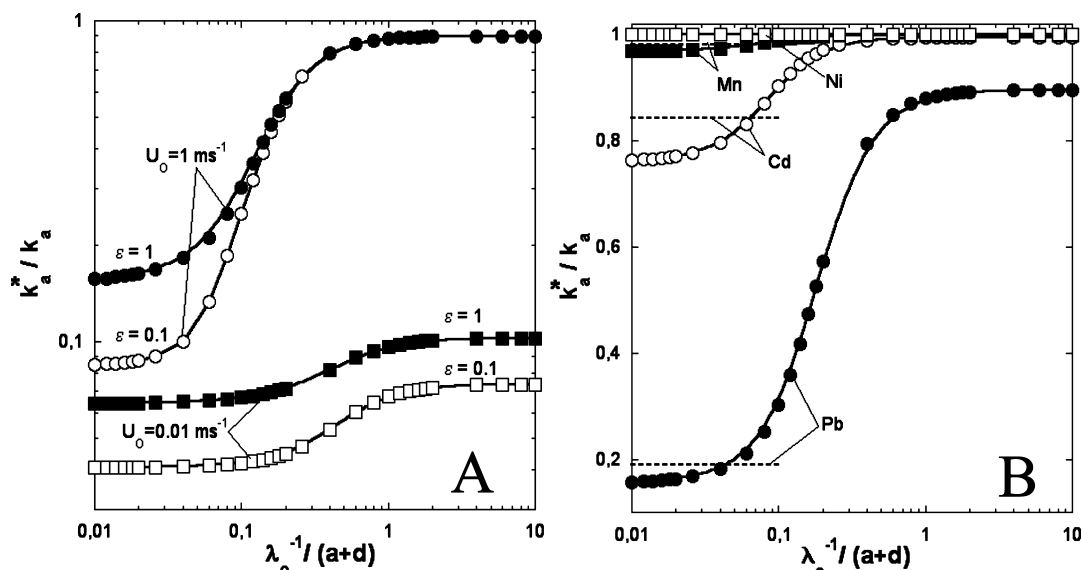


**Figure 10.** (A) Dependence of the ratio  $k_a^*/k_a$  on  $\lambda_o^{-1}$ ,  $\varepsilon = D_{M,\text{in}}/D_{M,\text{out}}$  and  $U_0$  (indicated) in the steady-state nonequilibrium chemical regime. Other model parameters as in Figure 3. (B) Ratio  $k_a^*/k_a$  in the time range that corresponds to the steady-state regime as a function of  $\lambda_o^{-1}$  for  $U_0 = 1 \text{ m s}^{-1}$  for lead(II), cadmium(II), manganese(II), and nickel(II) (indicated). Model parameters as in Figure 3 except  $k_w(\text{Pb}) = 7 \times 10^9 \text{ s}^{-1}$ ,  $k_w(\text{Cd}) = 3 \times 10^8 \text{ s}^{-1}$ ,  $k_w(\text{Mn}) = 3 \times 10^7 \text{ s}^{-1}$ , and  $k_w(\text{Ni}) = 3 \times 10^4 \text{ s}^{-1}$  recalling that  $k_a = K_{\text{os}}k_w^{14-16}$  and that  $K_{\text{os}}$  and  $k_w$  are tabulated values extracted from ref 6 (0.01 M ionic strength and  $z_M z_L = -2$  with  $z_M$  and  $z_L$  as the valence of M and L, respectively). In A and B, plain lines are only guides to the eye, and symbols represent the numerical results. Dotted lines in panel B pertain to  $k_a^*/k_a$  values obtained in the impermeable limit using eq 25.

conditions, upon increase of  $k_a$ , that is, from Ni(II) to Pb(II), the strong diffusion-limitation for the flux of free M outside the particle shell leads to a dramatic decrease of  $k_a^*/k_a$ , which reflects very different properties of the colloidal complex in terms of dynamics. Whereas the assimilation of  $k_a^*$  to  $k_a$  is appropriate for Ni(II), it is not acceptable for metal ions with faster kinetic reactions (i.e., larger  $k_a$ ) and therefore significantly transport-limited speciation.

#### 4. Conclusions

The dynamic properties of colloidal complexes issued from the interaction of metals with soft (core–shell) ligand particles

are examined under conditions where particle dispersion is subjected to steady-state laminar hydrodynamic flow. The analysis is carried out on the basis of a theory for fluid dynamics in porous particles in conjunction with a convection-diffusion-reaction formalism that accounts for the radial and angular metal M and complex ML concentration distributions within and/or outside the particle shell where ligands L are located. Overall, the results indicate for the first time that the dynamic character of the colloidal complex as a whole is strongly governed by the internal and external fluid flow structures, in particular, by the so-called hydrodynamic flow penetration length within the reactive particle shell. The model covers the limiting situations

of impermeable hard particles and free draining porous colloids and further applies to convective–diffusion situations defined by Péclet number  $Pe$  ranging from 0 to values as large as  $10^3$ . The fundamental differences between dynamics of speciation in homogeneous solutions of ligands and that within dispersion of particle-confined ligands are subsumed in the relevant effective kinetic rate constant  $k_a^*$ . The latter is determined by a complex interplay between particle geometry, fluid flow distribution within and outside the porous component of the particle as well as intraparticle M–ML interconversion kinetics (constants  $k_{a,d}$ ). It is demonstrated that colloidal complex ML becomes more dynamic upon increase of bulk flow velocity and/or particle permeability and that the larger the ligand particle size the more inert the resulting colloidal complex. Also, in the presence of significant flow, the respective kinetic and transport contributions to the overall speciation process vary in a nonmonotonous manner with the core-to-particle size ratio as a result of intricate intertwined internal flow field distribution and radial diffusion transport of metal to the particle. Through the manuscript, the rigorous numerical results are discussed upon comparison with analytical expression of  $k_a^*$  valid for  $Pe = 0$  and for  $Pe > > 1$  in the limit of reduced particle permeability.

The current study is of importance for defining the lability criteria of colloidal ligand particles immersed in a large scale diffusion layer developed in the vicinity of a consuming macroscopic interface (like an electrode or microorganism) along which a tangential hydrodynamic flow field is present (either externally applied, as within the context of electrokinetics, or present in aquatic media, e.g., in flowing rivers). Such situations are ubiquitous in nature, analytical device, or industrial processes. The current results underpin the necessity to correct the lability criteria of the colloidal complex not only by replacing the large scale diffusion layer thickness by the appropriate power-law dependence on flow magnitude and diffusion coefficient but also by substituting the molecular reaction kinetic constant  $k_a$  by its colloidal counterpart  $k_a^*$  that includes the refined details of fluid flow structure inside and outside the ligand particles.

**Acknowledgment.** We gratefully thank Mr. Ye Ai from the Department of Aerospace Engineering, Old Dominion University, Norfolk, NV, for his help on the development of the COMSOL simulation codes. S.Q. also thanks the support by Ministry of Education, Science and Technology of Korea World Class University (WCU) Program.

**Supporting Information Available:** (i) Detailed steps for the derivation of eq 25. (ii) Analytical formulation of the hydrodynamic problem under conditions where  $Re < < 1$ . (iii) Time evolution of the ratio  $k_a^*/k_a$  for the particle geometry of Figure 3 and various values of  $\lambda_o^{-1}$  and  $U_o$ . (iv) Graphical representations of the angular and radial M and ML concentration distributions under conditions of Figure 4 and Figure 5.

(v) Details of the simulation box used in Comsol Multiphysics. This information is available free of charge via the Internet at <http://pubs.acs.org>.

## References and Notes

- (1) Buffle, J. In *Complexation reactions in aquatic systems. An analytical approach*; Ellis Horwood: Chichester, 1988.
- (2) Buffle, J. Van Leeuwen, H. P. (Eds) In *Environmental Particles, Vol I, Part III: Reaction and transport of particles in aquatic systems (Chapters 10–13)*; Lewis Publishers, Inc., MI, 1992.
- (3) Köster, W.; Van Leeuwen, H. P. Physicochemical Kinetics and transport at biointerfaces: setting the stage. In *Physicochemical Kinetics and transport at biointerfaces, Chapter 1*; Köster, W., Van Leeuwen, H. P., Eds.; John Wiley and Sons, Ltd.: Chichester, 2004.
- (4) Van Leeuwen, H. P. *Environ. Sci. Technol.* **1999**, *33*, 3743.
- (5) Mota, A. M. Correia dos Santos, M. M. In *Metal speciation and Bioavailability*; Tessier, A., Turner, D., Eds.; Chapter 5, John Wiley and Sons: New York, 1995.
- (6) Pinheiro, J. P.; Minor, M.; Van Leeuwen, H. P. *Langmuir* **2005**, *21*, 8635.
- (7) Pinheiro, J. P.; Minor, M.; Van Leeuwen, H. P. *J. Electroanal. Chem.* **2006**, *587*, 284.
- (8) Zhang, Z.; Buffle, J.; Alemani, D. *Environ. Sci. Technol.* **2007**, *41*, 7621.
- (9) Duval, J. F. L.; Pinheiro, J. P.; Van Leeuwen, H. P. *J. Phys. Chem. A* **2008**, *112*, 7137.
- (10) Duval, J. F. L. *J. Phys. Chem. A* **2009**, *113*, 2275.
- (11) Duval, J. F. L. In *Environmental Colloids and Particles: Behaviour, Separation and Characterization Vol. 10, Chapter 7: Electrophoresis of soft colloids: basic principles and applications*; K. J. Wilkinson, J. Lead., Eds.; John Wiley and Sons: Chichester, 2007.
- (12) Ohshima, H. *Adv. Colloid Interface Sci.* **1995**, *62*, 189.
- (13) Duval, J. F. L.; Ohshima, H. *Langmuir* **2006**, *22*, 3533.
- (14) Eigen, M. *Z. Phys. Chem.* **1954**, *1*, 176.
- (15) Morel, F. M. M. Hering, J. G. In *Principles and applications of aquatic chemistry*; John Wiley: New York, 1993.
- (16) Van Leeuwen, H. P. *J. Radioanal. Nucl. Chem.* **2000**, *246*, 487.
- (17) Buffle, J.; Zhang, Z.; Startchev, K. *Environ. Sci. Technol.* **2007**, *41*, 7609.
- (18) Duval, J. F. L.; Wilkinson, K. J.; van Leeuwen, H. P.; Buffle, J. *Environ. Sci. Technol.* **2005**, *39*, 6435.
- (19) Rotureau, E.; Thomas, F.; Duval, J. F. L. *Langmuir* **2007**, *23*, 8460.
- (20) Gaboriaud, F.; Gee, M. L.; Strugnell, R.; Duval, J. F. L. *Langmuir* **2008**, *24*, 10988.
- (21) Shamrock, V. J.; Duval, J. F. L.; Lindsey, G. G.; Gaboriaud, F. *FEMS Yeast Res.* **2009**, *9*, 391.
- (22) Langlet, J.; Gaboriaud, F.; Gantzer, C.; Duval, J. F. L. *Biophys. J.* **2008**, *94*, 3293.
- (23) Brinkman, H. C. *Appl. Sci. Res.* **1947**, *A1*, 27.
- (24) Debye, P.; Bueche, A. *J. Chem. Phys.* **1948**, *16*, 573.
- (25) Sangani, S. A.; Yao, C. *Phys. Fluids* **1988**, *31*, 2435.
- (26) Duval, J. F. L.; Zimmermann, R.; Cordeiro, A. L.; Rein, N.; Werner, C. *Langmuir* **2009**, *25*, 10691.
- (27) Kim, S.; Russel, W. B. *J. Fluid Mech.* **1985**, *154*, 269–286.
- (28) Happel, J. *AIChE J.* **1958**, *4*, 197–201.
- (29) Neale, G. H.; Nader, W. K. *AIChE J.* **1974**, *20*, 530–538.
- (30) Carman, P. C. In *Flow of gases through porous media*; Academic Press: New York, 1956.
- (31) Fatin-Rouge, N.; Milon, A.; Buffle, J.; Goulet, R. R.; Tessier, A. *J. Phys. Chem. B* **2003**, *107*, 12126.
- (32) Deuflhard, P. *Numer. Math.* **1974**, *22*, 289.
- (33) Brown, P. N.; Hindmarsh, A. C.; Petzold, L. R. *SIAM J. Sci. Comput.* **1994**, *15*, 1467.
- (34) Levich, V. G. In *Physicochemical hydrodynamics*; Prentice Hall: Englewood Cliffs, NJ, 1962.

JP9068976

## SUPPORTING INFORMATION

### Metal speciation dynamics in dispersions of soft colloidal ligand particles under steady-state laminar flow condition

Jérôme F.L. Duval,<sup>1\*</sup> Shizhi Qian<sup>2,3</sup>

<sup>1</sup> Laboratory Environment and Mineral Processing, Nancy-University, CNRS, BP 40 – F-54501 Vandoeuvre-lès-Nancy Cedex, France.

<sup>2</sup> Department of Aerospace Engineering, Old Dominion University, Norfolk, VA, USA.

<sup>3</sup> School of Mechanical Engineering, Yeungnam University,  
Gyongsan 712-749, South Korea.

**I. Demonstration of the analytical expression (eq 25) for  $k_a^*$  under the conditions  $Pe \gg 1$ ,  $Re \gg 1$  and  $d \ll a$  in steady-state non-equilibrium chemical regime.**

The integration of both sides of eq 11 over the volume of the soft surface layer leads to

$$\frac{\partial \rho_{ML}^s(t)}{\partial t} = -k_d \rho_{ML}^s(t) + k_a \rho_M^s(t) c_L^*, \quad (S1)$$

where we have introduced the smeared-out concentrations  $\rho_{i=ML}^s$  over the shell layer volume of the particle as follows

$$i = M, ML: \quad \rho_i^s(t) = \frac{2\pi}{V_s} \int_a^{a+d} \int_0^\pi r^2 c_i(t, r, \theta) \sin \theta dr d\theta, \quad (S2)$$

with  $V_s = 4\pi \left\{ (a+d)^3 - a^3 \right\} / 3$  the volume over which the reactive binding sites L are homogeneously distributed. Multiplication of both sides of eq S1 by the ratio  $V_s / V_c$  leads to

$$\frac{\partial \rho_{ML}^V(t)}{\partial t} = -k_d \rho_{ML}^V(t) + k_a \rho_M^s(t) \rho_L^V \quad (S3)$$

, where we recall that the smeared-out concentration  $\rho_L^V$  over the shell layer volume is  $\rho_L^V = c_L^*$ , and

$$i = L, ML: \quad \rho_i^V / \rho_i^s = V_s / V_c \quad (S4)$$

Under conditions of large Péclet number and for sufficiently thin layer shell  $d \ll a$ , the free metal concentration can be taken as constant within the thin layer shell, *i.e.* we may neglect the angular and radial polarizations of  $c_M$  within particle shell so that, in turn,

$$\rho_M^s(t) \approx c_M(t, r = a + d). \text{ Equation S3 then simplifies into}$$

$$\frac{\partial \rho_{ML}^V(t)}{\partial t} = -k_d \rho_{ML}^V(t) + k_a c_M(t, r = a + d) \rho_L^V. \quad (\text{S5})$$

In line with the condition  $Pe >> 1$ , following the argument first advanced by Levich,<sup>1</sup> we may omit the angular component  $\frac{1}{r^2 \sin \theta} \frac{\partial}{\partial \theta} \left( \sin \theta \frac{\partial c_M}{\partial \theta} \right)$  in the Laplacian of the free metal concentration because derivatives along the particle surface are small as compared to those along the radius vector. Equation 12 then becomes

$$\begin{aligned} \frac{\partial c_M(t, r, \theta)}{\partial t} = D_{M,in} \left( \frac{\partial^2 c_M(t, r, \theta)}{\partial r^2} + \frac{2}{r} \frac{\partial c_M(t, r, \theta)}{\partial r} \right) + \left\{ k_d c_{ML}(t, r, \theta) - k_a c_M(t, r, \theta) c_L^* \right\} \\ - \vec{u}(r, \theta) \cdot \nabla c_M(t, r, \theta) \end{aligned} \quad (\text{S6})$$

Summation of eqs 11 and S6 and subsequent integration over the shell volume provides

$$\begin{aligned} \frac{\partial}{\partial t} \left\{ \rho_{ML}^s(t) + \rho_M^s(t) \right\} \approx \frac{2\pi D_{M,in}}{V_s} \int_0^\pi \sin \theta \left[ (a+d)^2 \frac{\partial c_M(t, r, \theta)}{\partial r} \Big|_{r=a+d} - a^2 \frac{\partial c_M(t, r, \theta)}{\partial r} \Big|_{r=a} \right] d\theta \\ - \frac{2\pi}{V_s} \int_a^{a+d} \int_0^\pi r^2 \vec{u}(r, \theta) \cdot \nabla c_M(t, r, \theta) \sin \theta dr d\theta \end{aligned} \quad (\text{S7})$$

where we have used the relation

$$\int_a^{a+d} r^2 \nabla^2 c_M(t, r, \theta) dr = (a+d)^2 \frac{\partial c_M(t, r, \theta)}{\partial r} \Big|_{r=a+d} - a^2 \frac{\partial c_M(t, r, \theta)}{\partial r} \Big|_{r=a}. \quad (\text{S8})$$

The zero flux condition at the core particle surface (eq 17) together with the no-slip condition expressed by eq 6 and the neglect of angular polarization for free metal concentration in the (immortal) thin shell ( $d \ll a$ ) further yields  $\partial c_M(t, r, \theta)/\partial r \approx 0$  and  $\vec{u}(r, \theta) \cdot \nabla c_M(t, r, \theta) \approx 0$  for  $a \leq r < a + d$ ,  $\forall \theta$ . Substituting these expressions into eq S7, multiplying both sides by  $c_p V_s$  and recalling that  $c_p V_s \rightarrow 0$  for  $r_c \rightarrow \infty$  (dilute suspensions are considered here), it comes

$$\frac{\partial \rho_{\text{ML}}^V(t)}{\partial t} \approx 2\pi(a+d)^2 D_{\text{M,in}} c_p \int_0^\pi \sin \theta \left. \frac{\partial c_{\text{M}}(t, r, \theta)}{\partial r} \right|_{r=a+d} d\theta. \quad (\text{S9})$$

In quasi steady-state regime, the time variation of  $\rho_{\text{ML}}^V$  may be taken from the gradient of steady-state profile of free metal just outside the particle shell. The classical Levich expression for diffusional flux to a hard particle surface under laminar flow conditions at large Péclet numbers  $Pe >> 1$  and low Reynolds numbers  $Re << 1$ ,<sup>1</sup> is written

$$D_{\text{M}} \left. \frac{\partial c_{\text{M}}(t, r, \theta)}{\partial r} \right|_{r=a+d} = \frac{3^{2/3}}{\Gamma(1/3)} (a+d)^{-2/3} D_{\text{M}}^{2/3} U_o^{1/3} \times \frac{\sin \theta}{\left( \theta - \frac{\sin 2\theta}{2} \right)^{1/3}} \left[ c_{\text{M}}^* - c_{\text{M}}(t, r = a+d) \right], \quad (\text{S10})$$

where the diffusion coefficients of metal M are taken identical within and outside the shell  $D_{\text{M}} = D_{\text{M,in}} = D_{\text{M,out}}$ , and  $\Gamma$  is the gamma function. Substituting eq S10 into eq S9 and performing the integration, we obtain

$$\frac{\partial \rho_{\text{ML}}^V(t)}{\partial t} \approx \frac{(3\pi)^{5/3}}{2\Gamma(1/3)} (a+d)^{4/3} c_p D^{2/3} U_o^{1/3} \left[ c_{\text{M}}^* - c_{\text{M}}(t, r = a+d) \right] \quad (\text{S11})$$

Elimination of  $c_{\text{M}}(t, r = a+d)$  from eq S5 and substitution in eq S11 finally leads to

$$\frac{\partial \rho_{\text{ML}}^V(t)}{\partial t} \approx \left( 1 + \frac{k_a \rho_L^V}{\frac{(3\pi)^{5/3}}{2\Gamma(1/3)} (a+d)^{4/3} c_p D^{2/3} U_o^{1/3}} \right)^{-1} \left( -k_d \rho_{\text{ML}}^V(r, t) + k_a c_{\text{M}}^* \rho_L^V \right). \quad (\text{S12})$$

Identification of eq S12 with eq 22 immediately gives eq 25 providing  $\rho_{\text{M}}^V \approx c_{\text{M}}^*$ , which is justified for very dilute colloidal ligand suspensions (as verified *a posteriori* from the rigorous numerical analysis of the local M concentration profiles within and outside the particle shell).

## II. Analytical formulation of the flow field distribution for $Re << 1$ .

For Reynolds number  $Re << 1$ , eq 2 in the main text becomes the Stokes equation

$$r \geq a+d : \quad -\nabla \cdot pI + \eta \nabla^2 \vec{u} = \vec{0}. \quad (\text{S13})$$

Following the classical strategy adopted in fluid dynamic computation,<sup>1-3</sup> we take advantage of the continuity equation 4 to define the stream function  $\psi(r, \theta)$  according to

$$u_r(r, \theta) = -1/(r^2 \sin \theta) \partial \psi(r, \theta) / \partial \theta \quad \text{and} \quad u_\theta(r, \theta) = 1/(r \sin \theta) \partial \psi(r, \theta) / \partial r. \quad (\text{S14,S15})$$

Then, taking the curl (operator  $\nabla \times$ ) of eq S13, eliminating the pressure term and substituting eqs S14, S15, we obtain the biharmonic equation

$$r \geq a + d : \quad E^4 \psi = 0. \quad (\text{S16})$$

where  $E$  is the operator defined by  $E^2 = \partial^2 / \partial r^2 + (\sin \theta / r^2) \frac{\partial}{\partial \theta} \left( \frac{1}{\sin \theta} \frac{\partial}{\partial \theta} \right)$ . Similarly, it is shown that the local flow field distribution within the shell is governed by the differential equation

$$a \leq r \leq a + d : \quad E^4 \psi - \lambda_o^2 E^2 \psi = 0. \quad (\text{S17})$$

Solutions of eq S16 and S17 may be found by separating the variables  $r$  and  $\theta$  according to  $\psi^*(r, \theta) = \psi(r, \theta) / [U_o(a+d)^2] = f(r) \sin^2 \theta$ . Equations S16 and S17 are then written in term of the dimensionless function  $f(r)$  as follows

$$x \geq 1 : \quad f^{(4)}(x) - \frac{4}{x^2} f^{(2)}(x) + \frac{8}{x^3} f^{(1)}(x) - \frac{8}{x^4} f(x) = 0. \quad (\text{S18})$$

$$\frac{a}{R} \leq x \leq 1 : \quad f^{(4)}(x) - \left[ \frac{4}{x^2} + (\lambda_o R)^2 \right] f^{(2)}(x) + \frac{8}{x^3} f^{(1)}(x) + \left[ \frac{2(\lambda_o R)^2}{x^2} - \frac{8}{x^4} \right] f(x) = 0, \quad (\text{S19})$$

where  $x = r/R$ ,  $R = a + d$  and  $f^{(1 \leq n \leq 4)}$  the n-th derivative of the function  $f$  with respect to  $x$ .

The general solution of eq S18 reads as<sup>3,4</sup>

$$x \geq 1 : \quad f(x) = \frac{\alpha_1}{x} + \alpha_2 x + \alpha_3 x^2 + \alpha_4 x^4. \quad (\text{S20})$$

Additionally, eq S19 admits as general solution<sup>3,5</sup>

$$\frac{a}{R} \leq x \leq 1 : \quad f(x) = \frac{\alpha_5}{x} + \alpha_6 x^2 + \alpha_7 \left[ \frac{\cosh(\lambda_o Rx)}{\lambda_o Rx} - \sinh(\lambda_o Rx) \right] + \alpha_8 \left[ \frac{\sinh(\lambda_o Rx)}{\lambda_o Rx} - \cosh(\lambda_o Rx) \right], \quad (\text{S21})$$

where  $\alpha_{1 \leq i \leq 8}$  are constants to be determined from the boundaries given by eqs 5-10, recalling that formulation of the problem in terms of the dimensionless stream function  $\psi^*(r, \theta)$  necessarily satisfies eq 4. Using eqs S14-S15, the far field condition expressed by eq 5 reduces to

$\psi(r \rightarrow \infty, \theta) \rightarrow -U_o r^2 \sin^2 \theta / 2$  or equivalently  $f(x \rightarrow \infty) \rightarrow -x^2 / 2$ . The latter expression allows direct determination of  $\alpha_{3,4}$

$$\alpha_3 = -1/2 \text{ and } \alpha_4 = 0. \quad (\text{S22,S23})$$

The next step consists in expressing the 5 remaining boundaries 6-10 in terms of  $\psi^*(r, \theta)$  or equivalently  $f(x)$  so as to evaluate the undetermined constants  $\alpha_{1,2,5,6,7,8}$ . The no-slip condition (eq 6) at the core particle surface provides

$$f(x = a/R) = 0 \text{ and } f^{(1)}(x = a/R) = 0. \quad (\text{S24,S25})$$

The continuity of the radial velocity component at  $r = a + d$  (eq 7) imposes

$$f(x = 1^+) = f(x = 1^-), \quad (\text{S26})$$

while that of the tangential component (eq 8) gives

$$f^{(1)}(x = 1^+) = f^{(1)}(x = 1^-). \quad (\text{S27})$$

Given eqs S26-S27, the continuity at  $r = a + d$  of the tangential component of the stress tensor

$$(\text{eq 10}) \sigma_{r\theta} = \frac{\eta U_o \sin \theta}{R} \left[ \frac{f^{(2)}}{x} - \frac{2f^{(1)}}{x^2} + \frac{2f}{x^3} \right] \text{ necessarily requires}$$

$$f^{(2)}(x = 1^+) = f^{(2)}(x = 1^-). \quad (\text{S28})$$

Because eq S26 reflects continuity of the radial velocity, continuity of the normal stress  $\sigma_{rr} = -p + 2\eta \frac{\partial u_r}{\partial r}$  is ensured providing the pressure  $p$  or equivalently  $\partial p / \partial \theta$  is continuous at  $x = 1$ .<sup>3</sup> Taking the expressions derived in ref 3 for  $\partial p / \partial \theta$ , and using eqs S26-S27, we finally obtain

$$f^{(3)} - (\lambda_o R)^2 f^{(1)} \Big|_{x=1^-} = f^{(3)} \Big|_{x=1^+}. \quad (\text{S29})$$

Making use of eqs S20-S29, we show that the constants  $\alpha_{1,2,5,6,7,8}$  are solutions of the matricial equation

$$T \cdot \vec{S} = \vec{C}, \quad (\text{S30})$$

where  $\vec{S}$  and  $\vec{C}$  are the column vectors defined by

$$\vec{S} = \begin{pmatrix} \alpha_1 \\ \alpha_2 \\ \alpha_5 \\ \alpha_6 \\ \alpha_7 \\ \alpha_8 \end{pmatrix}, \quad \vec{C} = \begin{pmatrix} 1/2 \\ 1 \\ 1 \\ 0 \\ 0 \\ 0 \end{pmatrix} \quad (S31)$$

and  $T$  the  $6 \times 6$  matrix

$$T = \begin{pmatrix} 1 & 1 & -1 & -1 & -g_3(1) & -g_4(1) \\ -1 & 1 & 1 & -2 & -g_3^{(1)}(1) & -g_4^{(1)}(1) \\ 2 & 0 & -2 & -2 & -g_3^{(2)}(1) & -g_4^{(2)}(1) \\ -6 & 0 & 6 - (\lambda_o R)^2 & 2(\lambda_o R)^2 & -g_3^{(3)}(1) + g_3^{(1)}(1)(\lambda_o R)^2 & -g_4^{(3)}(1) + g_4^{(1)}(1)(\lambda_o R)^2 \\ 0 & 0 & (a/R)^{-1} & (a/R)^2 & g_3(a/R) & g_4(a/R) \\ 0 & 0 & -(a/R)^{-2} & 2a/R & g_3^{(1)}(a/R) & g_4^{(1)}(a/R) \end{pmatrix} \quad (S32)$$

with the functions  $g_3$  and  $g_4$  given by

$$g_3(x) = \frac{\cosh(\lambda_o Rx)}{\lambda_o Rx} - \sinh(\lambda_o Rx), \quad (S33)$$

and

$$g_4(x) = \frac{\sinh(\lambda_o Rx)}{\lambda_o Rx} - \cosh(\lambda_o Rx). \quad (S34)$$

Equations S31-S34 were solved by *LU* decomposition of the matrix  $T$  and subsequent determination of the solutions of the resulting triangular set of equations was achieved by classical forward substitution and back substitution techniques. From the so-obtained  $\alpha_{1,2,5,6,7,8}$  constants, we could determine the stream function profiles. The latter could be further successfully compared with those obtained from direct numerical evaluations of eqs S18-S19 (with boundaries S24-S29 and with that expressing the far-field condition) making use of the collocation method.<sup>6</sup> The hydrodynamic flow field profiles obtained as detailed in §2.2 of the main text under condition  $Re \ll 1$ , agree very well with those determined according to the analytical formulation of the flow problem detailed above. In particular, the limits of impermeable and free draining shell, as met for  $\lambda_o^{-1} \ll d$  and  $\lambda_o^{-1} \gg d$ , respectively, could be reproduced. For the former case, there is no flow within the shell and one easily verifies

that for  $x \geq 1$ ,  $f$  reduces to  $f(x) = -\frac{1}{4x} + \frac{3}{4}x - \frac{1}{2}x^2$ . Similar expression is obtained for the situation where  $\lambda_0^{-1} \gg d$  upon defining  $x$  by the ratio  $r/a$ .

### III. Supporting Figures.

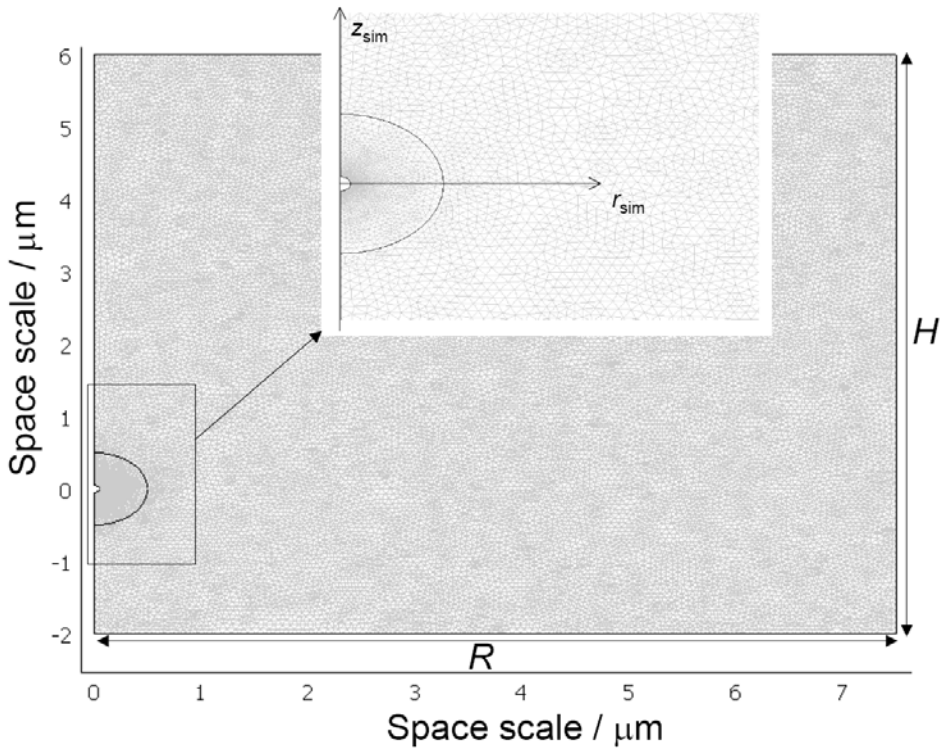


**Figure S1.** Typical simulation box used within Comsol Multiphysics environment for the evaluation of the velocity field and local M and ML concentrations. For the sake of convenience, calculations were performed in *axial-symmetric cylindrical geometry* in the coordinate system ( $r_{\text{sim}}$ ,  $z_{\text{sim}}$ ) as indicated in the figure. Because of symmetry argument, the problem is indeed invariant upon rotation around the axis  $r_{\text{sim}}=0$ . It was systematically verified that the obtained numerical solutions were independent of the size/local density of the chosen mesh (an example of which is given in the figure) and size of the simulation box as subsumed in the variables  $R$  and  $H$ . The situation is therefore that of a spherical colloidal ligand particle enclosed in a cylinder of height  $H$  and radius  $R$ . Computations of the various volume concentrations involved in the expression of  $k_a^*$  (eq 23 in the main text) were of course performed using the appropriate integral definition of these variables in cylindrical geometry. It is emphasized that performing the simulation in a cylinder of infinitely large radius and large height at the center of which the ligand particle is placed (Figure S1, ( $r_{\text{sim}}$ ,  $z_{\text{sim}}$ ) coordinate system), is equivalent to carrying out the computation in an infinitely large spherical cell that contains the particle (Figure 1, ( $r, \theta$ ) coordinate system), recalling that hydrodynamic interactions between particles are ignored in the study (infinitely dilute suspensions only are considered).

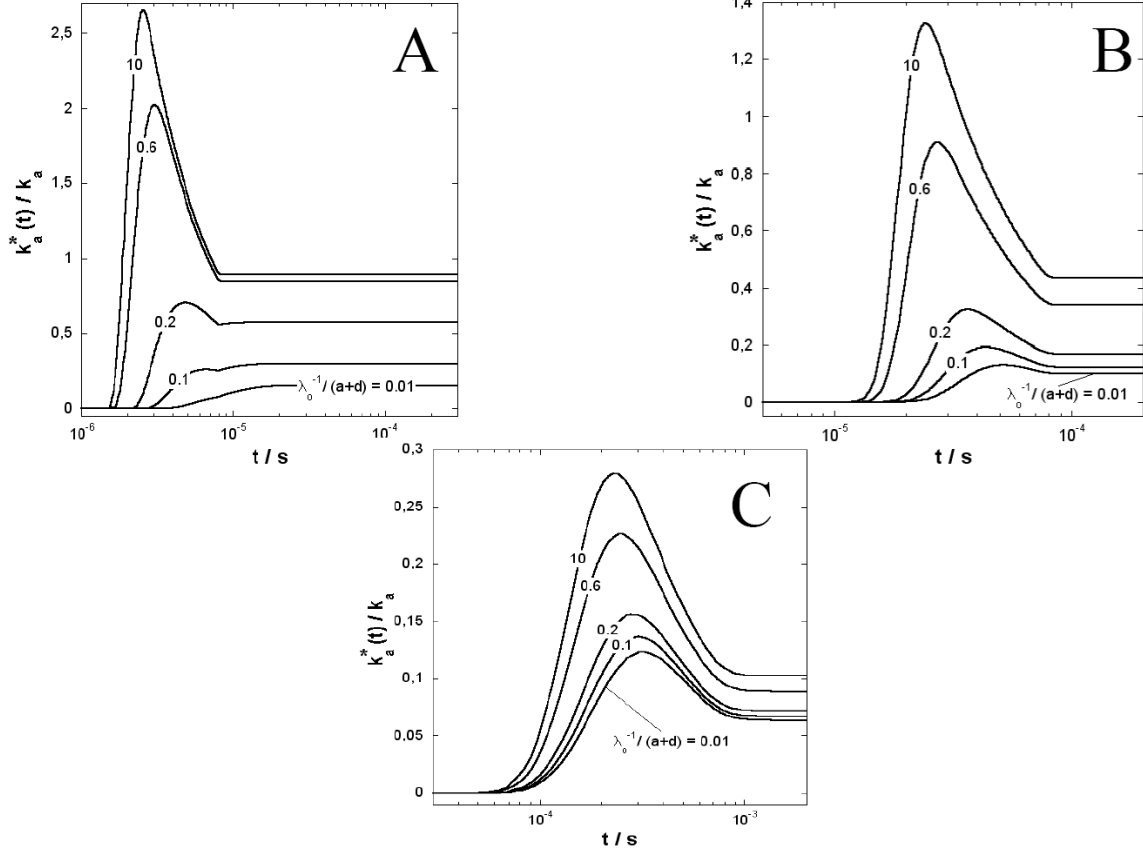


**Figure S2.** Time evolution of the ratio  $k_a^*/k_a$  for various  $\lambda_0^{-1}/(a+d)$  (indicated) for (A)  $U_o = 1 \text{ m s}^{-1}$  ( $Pe = 500$ ), (B)  $U_o = 10^{-1} \text{ m s}^{-1}$  ( $Pe = 50$ ) and (C)  $U_o = 10^{-2} \text{ m s}^{-1}$  ( $Pe = 5$ ). Other model parameters as in Figure 3 of the main text. Panel B corresponds to the hydrodynamic conditions for which the M and ML concentration distributions are depicted in Figure 3 of the main text. The time required to reach steady-state regime is a function of the velocity  $U_o$  that governs the speed of approach of free metals M toward the shell. The dependences of  $k_a^*/k_a$  on  $U_o$  and  $\lambda_0^{-1}$  in the steady-state regime are extensively discussed in the text (Figure 6). Qualitatively, the peculiar time-dependence of  $k_a^*/k_a$ , in particular the presence of a maximum, is analogous to that commented in ref 7. The form of the maximum in  $k_a^*/k_a$  is depending on  $U_o$  and  $\lambda_0^{-1}$ : the larger  $\lambda_0^{-1}$ , the broader is the aforementioned peak and the larger  $U_o$ , the sharper it becomes.

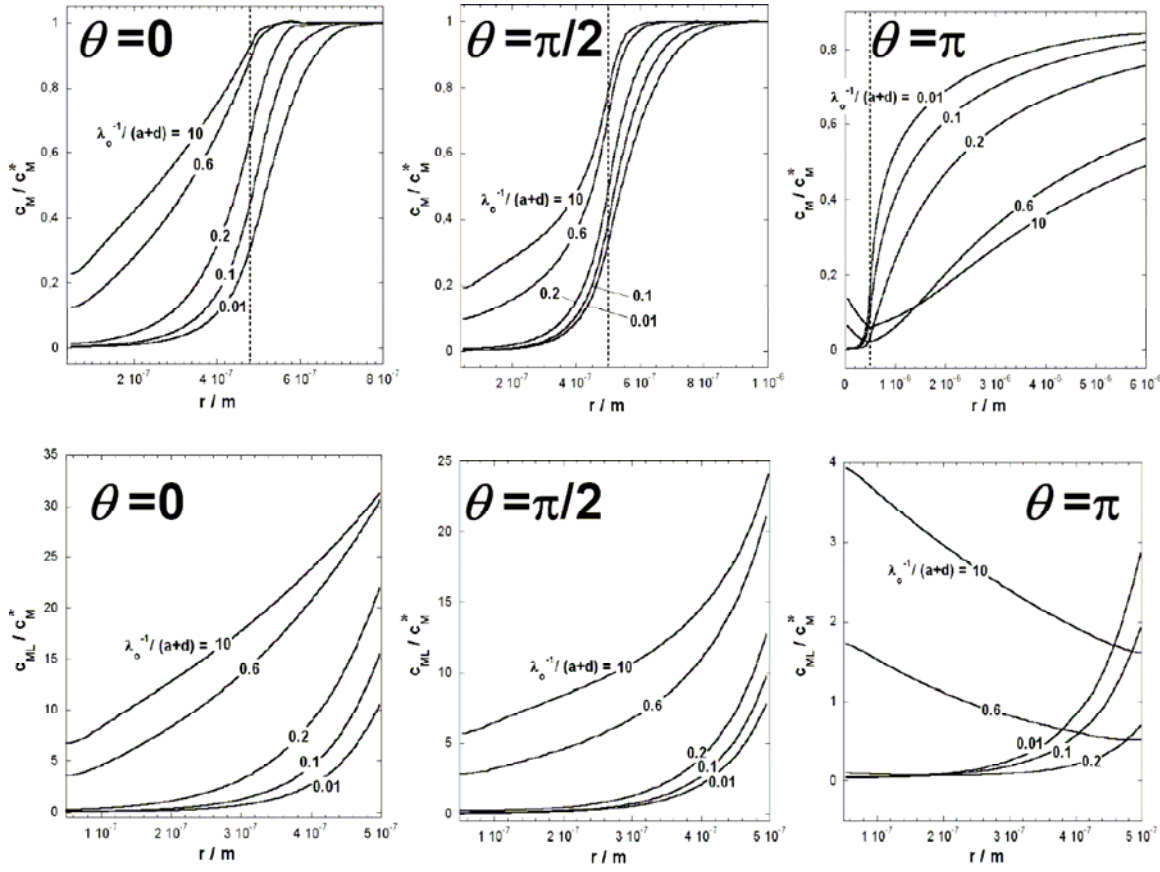


**Figure S3.** M (top figures) and ML (down figures) concentration distributions within (for ML) and/or outside (for M) the shell in the steady-state non-equilibrium chemical regime for various  $\lambda_0^{-1}$  (indicated) and three values of  $\theta$  (indicated). Other model parameters as in Figure 3 of the main text. The dotted line indicates the position of the interface between shell and outer solution (*i.e.*  $r = a + d$ ). Figure S3 corresponds to the M/ML concentration contour surfaces depicted in Figure 4 of the main text.

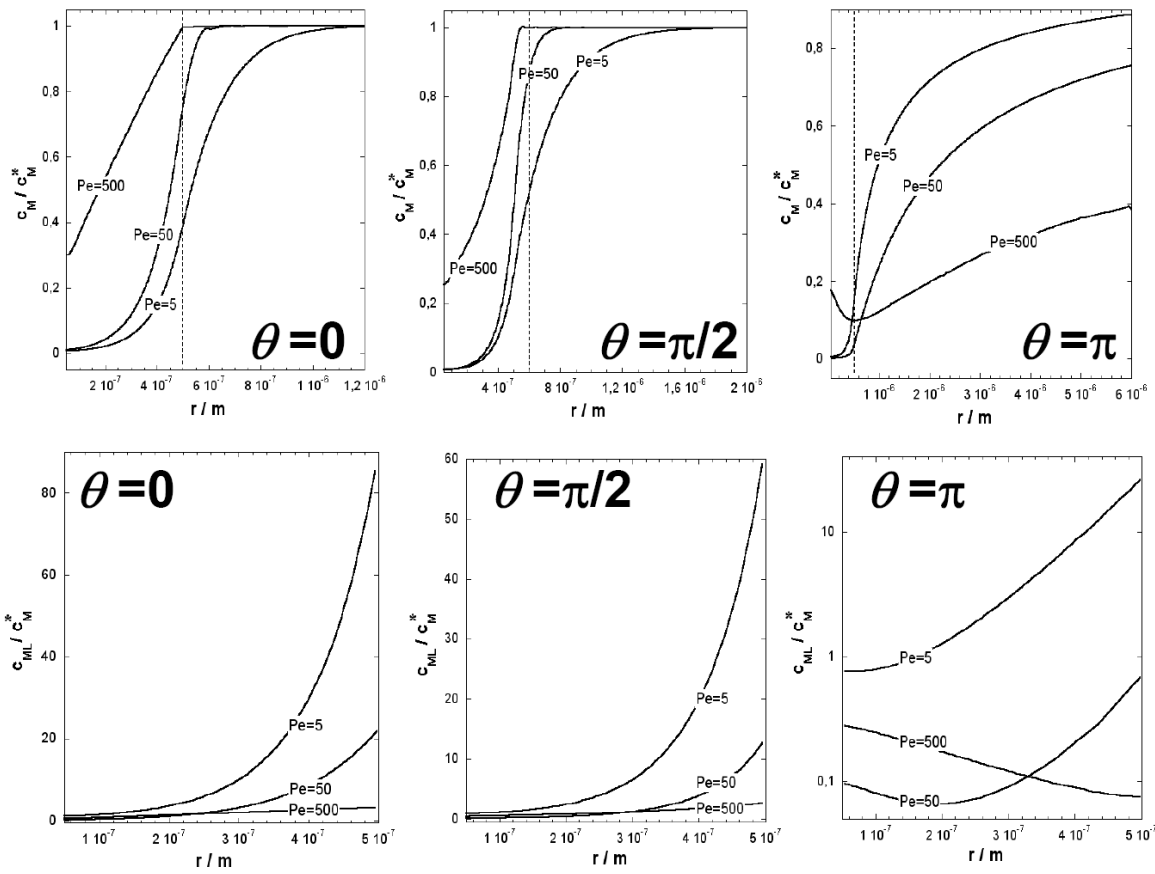


**Figure S4.** M (top figures) and ML (down figures) concentration distributions within (for ML) and/or outside (for M) the shell in the steady-state non-equilibrium chemical regime for various  $U_o$  (or  $Pe$ , indicated) and three values of  $\theta$  (indicated). Other model parameters as in Figure 3 of the main text. The dotted line indicates the position of the interface between shell and outer solution (*i.e.*  $r = a + d$ ). Figure S4 corresponds to the M/ML concentration contour surfaces depicted in Figure 5 of the main text.

### References and Notes.

- (1) Levich, V.G. In *Physicochemical hydrodynamics*; Prentice Hall, Englewood Cliffs, NJ, 1962.
- (2) Ganapathy, R. *Z. angew. Math. Mech.* **1997**, 77, 871.
- (3) Vanni, M. *Chem. Eng. Sci.* **2000**, 55, 685.
- (4) Happel, J.; Brenner, H. In *Low Reynolds number hydrodynamics*. Prentice Hall, Englewood Cliffs, NJ, 1965.
- (5) Nandakumar, K.; Masliyah, J.H. *Can. J. Chem. Eng.* **1982**, 60, 202-211.
- (6) Ascher, U.; Christiansen, J.; Russel, R.D. *ACM T. Math. Software* **1981**, 7, 209-222.
- (7) Duval, J.F.L.; Pinheiro, J.P.; Van Leeuwen, H.P. *J. Phys. Chem. A* **2008**, 112, 7137.